Electrocatalytic CO₂ Reduction to Formate with Molecular Fe(III) Complexes Containing Pendent Proton Relays

Asa W. Nichols, Shelby L. Hooe, Joseph S. Kuehner, Diane A. Dickie, and Charles W. Machan*

* - machan@virginia.edu; ORCID: 0000-0002-5182-1138

Department of Chemistry, University of Virginia, PO Box 400319, Charlottesville, Virginia 22904-4319, United States

Abstract

Previously, we reported an iron (III) complex with 6,6'-([2,2'-bipyridine]-6,6'-diyl)bis(2,4-ditertbutyl-phenol) as a ligand (Fe(^{tbu}dhbpy)Cl, **1**) as a catalyst for the electrochemical reduction of CO_2 to formate (Faradaic efficiency $FE(HCO_2^-)$ = 68±4%). In mechanistic experiments, an essential component was found to be a pre-equilibrium involving the association of the proton donor with the catalyst, which preceded proton transfer to the Fe-bound O atoms upon reduction of the Fe center. Here, we report the synthesis, structural characterization, and reactivity of two iron(III) compounds with 6,6'-([2,2'-bipyridine]-6,6'-diyl)bis(4-(methyl)-2-methoxyphenol) (^{me}crebpy[H]₂, Fe(^{me}crebpy)Cl, **2**) and 6,6'-([2,2'-bipyridine]-6,6'-diyl)bis(4-(tert-butyl)benzene-1,2-diol) (^{tbu}catbpy[H]₄, Fe(^{tbu}catbpy), **3**) as ligands, where pendent –OMe and –OH groups are poised to modify the protonation reaction involving the Fe-bound O atoms. Differences in selectivity and activity for the electrocatalytic reduction of carbon dioxide (CO_2) to formate (HCO_2^-) between **1-3** were assessed via cyclic voltammetry (CV) and controlled potential electrolysis (CPE) experiments in *N,N*-dimethylformamide (*N,N*-DMF). Mechanistic studies suggest that the O atoms in the secondary coordination sphere are important for relaying exogeneous protons to the active site, enhancing the multi-site electron proton transfer (MS-EPT) activation of the catalysts, which leads to a twenty-six-fold TOF_{max} increase for **2** and nineteen-fold for **3** in comparison to **1**. These studies also suggest that there is a difference in the strength of the interaction between the pendent moiety and the sacrificial proton donor between **2** and **3**, resulting in improvements in

catalytic activity and efficiency. CPE experiments demonstrate an increased $FE(HCO_2^-) = 85\pm2\%$ for **2**, whereas **3** had a lower $FE(HCO_2^-) = 71\pm3\%$. These results indicate that using secondary sphere moieties to modulate metal-ligand interactions and MS-EPT reactivity in the primary coordination sphere can be a powerful strategy for modulating electrocatalytic activity and selectivity.

Introduction

The steadily increasing market share of electricity from renewable sources continues to generate interest in developing electrochemical transformations for storing energy in chemical bonds.[1] One compelling approach is to direct energy from these sources towards electrochemical transformations of CO_2, a byproduct of fossil fuel usage and a greenhouse gas, into useful fuel precursors and commodity chemicals.[1, 2] In comparison to molecular electrocatalysts developed for the reduction of CO_2 to CO, relatively few catalysts have been developed which selectively produce formate.[3-5] Formate is currently utilized as an organic hydride source,[6] directly in a fuel cells,[7] and as a H_2 storage material.[8]

Previously, we identified a molecular Fe(III) chloride complex based upon 6,6′-di(3,5-di-tert-butyl-2-hydroxybenzene)-2,2′-bipyridine (**Fe(^{tbu}dhbpy)Cl**, **Figure 1**, **1**) which produced formate (HCO_2^-) with a FE of $68\pm4\%$ from CO_2 in the presence of 0.5 M phenol (PhOH) with an $E_{cat/2}$ of -2.45 V vs Fc^+/Fc.[9] Mechanistic studies suggested that a non-catalytic electrochemical reaction was vital to the observed reactivity: the Fe-bound oxygen atoms underwent protonation upon the Fe(III)/(II) reduction, a type of multi-site electron and proton transfer (MS-EPT) reaction.[9-12] MS-EPT mechanisms involving ligand protonation upon metal redox changes in the primary coordination sphere are generally invoked for metal oxime and dithiolene complexes which catalytically generate hydrogen (H_2)[13-17]; similar mechanisms are underdeveloped for other substrates.[3] MS-EPT has been explored broadly in photochemical and chemical systems, including the photosynthetic oxidation of tyrosine-Z,[18] ruthenium-based model compounds for phenol oxidation,[19] and

mixed TEMPOH/organic base/chemical oxidant systems.[20] Under electrochemical conditions, MS-EPT has also been studied as an oxidant for tyrosine by $[M(bpy)_3]^{3+/2+}$ systems (M = Os, Ru, Fe, bpy = 2,2′-bipyridine).[21]
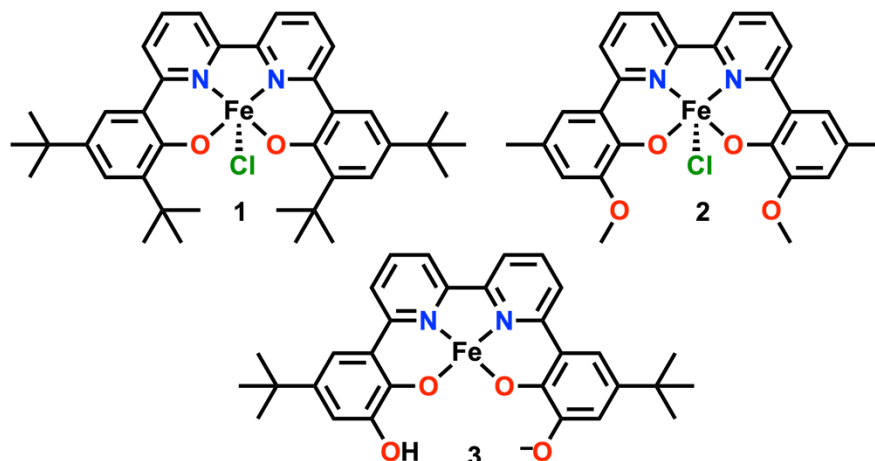
Figure 1. Molecular electrocatalysts for CO_2 reduction to formate (HCO_2^-) studied previously (**1**; Fe(tbudhbpy)Cl)[9] and in this work (**2**; Fe(mecrebpy)Cl and **3**; Fe(tbucatbpy)

A successful strategy for improving the activity, selectivity, and thermodynamic efficiency of molecular electrocatalysts which facilitate the transformation of CO_2 is the incorporation of pendent proton shuttles in the secondary coordination sphere of the respective complexes.[22-24] The utility of these functional groups holds for many electrocatalytic transformations: examples exist for the H_2 evolution,[25-27] oxygen reduction,[28-31] and CO_2 reduction[22, 32-35] reactions. In studies on molecular electrocatalysts for CO_2 reduction, the design emphasis is generally placed on positioning the pendent relay such that it can interact with CO_2 bound to the active site of the complex to stabilize intermediates, act as a proton relay, and/or to provide access to new reaction pathways to lower the energy input and increase catalytic rates.[22, 23, 35-37]

Intrigued by our initial observations of the MS-EPT reaction and its relationship to the catalytic response,[9] we have synthesized two new ligand frameworks containing secondary-sphere hydrogen bond-donor and -acceptor groups which are oriented to interact with the Fe-bound O atoms that are protonated upon reduction of the metal center (**Figure 1;** complexes **2** and **3**). By tuning the ability of the secondary sphere moiety to direct the exogenous sacrificial proton donor

to the metal-bound O atom, an increased TOF_{max} and selectivity for HCO_2^- is achieved. This demonstrates that non-catalytic MS-EPT reactions can be optimized via analogous strategies to those used for enhanced protonation rates of activated substrate at the metal center.

Here, we report the synthesis, structural, and electrochemical behavior of two new Fe(III) complexes containing pendent proton relays oriented to interact with the Fe-bound oxygen atoms of an N_2O_2 coordination environment. These complexes are based on the ligands 6,6'-([2,2'-bipyridine]-6,6'-diyl)bis(2-methoxy-4-methylphenol) (^{me}crebpy[H]$_2$, **Fe(^{me}crebpy)Cl, 2, Figure 1**) and 6,6'-([2,2'-bipyridine]-6,6'-diyl)bis(4-(tert-butyl)benzene-1,2-diol) (^{tbu}catbpy[H]$_4$, **Fe(^{tbu}catbpy), 3, Figure 1**). Initial studies have shown **2** to be an excellent catalyst for the reduction of CO_2 to HCO_2^-, with a twenty-six-fold enhancement in rate in comparison to **1** with 85±2% FE for HCO_2^-. In contrast, **3** is a more active catalyst than **1** with a nineteen-fold enhancement in rate, but no significant increase in is observed (FE **3** = 71±3%; FE **1** = 68±4%[9]). We believe the difference in reactivity for **2** comes from the advantageous interactions of the secondary sphere proton shuttle, exogeneous proton donor, and inner sphere Fe-bound oxygen atom, which contribute to a reaction rate enhancement and increase in selectivity.

Results

The isolation of the [^{me}crebpy(H)$_2$] and [^{tbu}catbpy(H)$_4$] ligands was accomplished through Pd-catalyzed cross-coupling procedures which are similar to the previously reported synthesis of [^{tbu}dhbpy(H)$_2$] (see **Experimental Methods**).[9] The corresponding Fe(III) complexes were obtained by refluxing the ligand in ethanol in the presence of equimolar $FeCl_3 \cdot H_2O$ with NaOAc as a proton scavenger. Single crystals of sufficient quality for X-ray diffraction studies were obtained for both **2** and **3** by the slow cooling of supersaturated acetonitrile solutions from refluxing temperatures. The solid-state structure of complex **2** is a dimeric species, with a single oxygen atom from each ligand framework coordinated to an axial position of a second Fe complex to create a hexadentate coordination environment (**Figure 2**). Likewise, complex **3** also exists as a dimeric species in the solid state, however in this case hexadentate coordination is instead

4

facilitated by the partial deprotonation of one of each of the catechol moieties per unit of **3** in the dimeric structure, replacing the Cl⁻ ligand for both Fe centers (**Figure S1**). Microanalysis of the as-synthesized **3** confirmed that complete chloride loss occurs for the bulk material, with charge for the Fe(III) center balanced by the deprotonation of one of the catechol moieties (**Figure 1; 3**). In both cases the solution-phase behavior suggests that these are monomeric species: diffusion coefficients for **2** and **3** determined by CV methods using the Randles-Sevcik equation are consistent with those determined for **1** and Fe-porphyrins (**Table S1**).[38] UV-Vis spectra of **2** and **3** obtained in *N,N*-DMF maintain linearity upon dilution, which is consistent with the absence of an equilibrium process **(Figure S2 and S3).** Finally, the magnetic moments determined by Evans' method of 5.9±0.1 and 6.0±0.1 BM obtained for **2** and **3**, respectively, are consistent with a monomeric high spin S = 5/2 Fe(III) species in each case.[9]
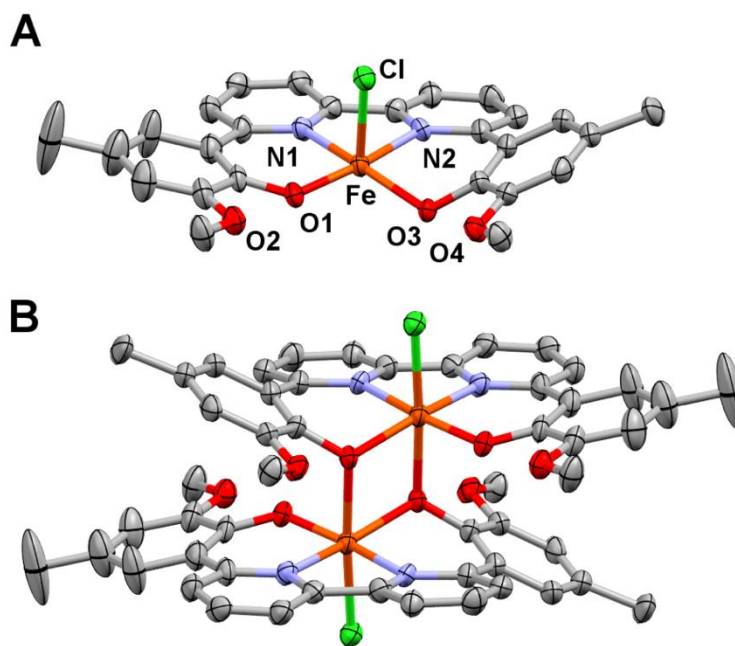
Figure 2. (**A)** Unit cell and **(B)** overall dimer structure for **2**; each equivalent of **2** is generated by symmetry and not crystallographically distinct. C = grey, O = red, N= blue, Fe = orange, Cl = green. Thermal ellipsoids set to 50%. Occluded acetonitrile molecules and hydrogen atoms omitted for clarity.

Electrochemical experiments conducted in 0.1 M TBAPF₆/*N,N*-DMF under Ar with each complex demonstrated redox processes at similar potentials to **1**.[9] Complex **2** exhibits one

irreversible 1e$^-$ reduction with $E_{p,a}$ = –1.45 V vs Fc$^+$/Fc and three reversible 1e$^-$ reductions with $E_{1/2}$ = –0.84, –1.93, and –2.55 V vs Fc$^+$/Fc, respectively (**Figure 3**, black). The irreversible reduction with $E_{p,a}$ = –1.45 V vs Fc$^+$/Fc disappears at fast scan rates upon the addition of TBACl as a source of Cl$^-$ (**Figure S4**), suggesting that it corresponds to the product of an equilibrium reaction involving Cl$^-$ loss. Complex **3** exhibits two reversible, 1e$^-$ reductions with $E_{1/2}$ = –1.01 V and –1.65 V vs Fc$^+$/Fc, respectively, followed by two one-electron reductions with $E_{1/2}$ = –2.24 V and $E_{p.a}$ = –2.58 V vs Fc$^+$/Fc (**Figure 3**, red). On the return sweep to oxidizing potentials with **3**, a feature with $E_{p,c}$ = –1.39 V vs Fc$^+$/Fc is observed when the CV switching potential is ~–2.7 V vs Fc$^+$/Fc, indicating that this CV feature is associated with the final two reduction waves (**Figure 3**, red). Interestingly, a scan rate-dependent relationship is observed between the final two reduction features for **3**. The reduction at –2.24 V vs Fc$^+$/Fc produces larger current densities at slow scan rates (<200 mV/s), but the reduction at –2.58 V vs Fc$^+$/Fc becomes more prominent at faster scan rates, at the expense of the more positive redox feature (**Figure S5**). This is indicative of an ECE mechanism, where at slower scan rates the intermediate chemical process which produces the first of these two features has sufficient time to occur.[39]
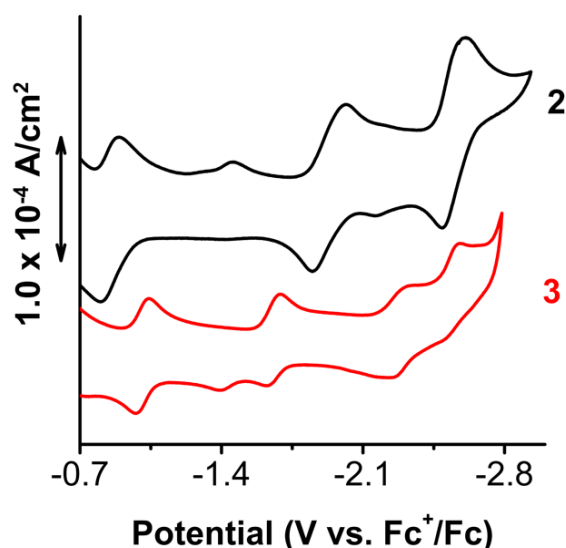
Figure 3. Cyclic Voltammograms of 0.5 mM **2** and **3** under an Ar atmosphere in 0.1 M TBAPF$_6$/*N,N*-DMF supporting electrolyte. Working electrode is glassy carbon, counter electrode is a glassy carbon rod, AgCl/Ag pseudoreference electrode. Referenced to internal decamethylferrocene (Cp$_2$*Fe) standard; 100 mV/s scan rate.

Variable scan rate experiments indicate the electrochemical response of both **2** and **3** is in a diffusion-limited regime for the first two reversible reductions (**Figures S6-S7**).[40] CVs of the corresponding Zn analogues of **2** and **3** show redox features only at potentials similar to the final two reductions for each, suggesting that the frontier orbital configuration in highly reduced states incorporates contributions from the ligand manifold (**Figures S8-S9**). As we have shown previously, the initial Fe(III)/(II) reduction feature is sensitive to the presence of a proton donor: for complex **2** (**Figure S10**) and complex **3** (**Figure S11**): distinct shifts to positive potentials and the coalescence of the more positive reduction features occur upon addition of PhOH as a proton donor. These changes are not conducive to the simple equilibrium modelling used previously,[41] which we attribute to multiple competing equilibria involving the pendent moieties, the Fe-bound O atoms and the proton donor at reducing potentials. In an attempt to deconvolute these processes, we examined the interactions between PhOH and both **2** and **3** using UV-vis spectroscopy, however, no well-defined isosbestic points were observed in the relevant concentration ranges (**Figures S12** and **S13**).

In the presence of CO_2 under aprotic conditions, **2** and **3** exhibit an increase in current, with i_p/i_c values of 5.5 and 13, respectively, with $E_{p,c}$ = –2.50 V and –2.37 V vs Fc^+/Fc, respectively (**Figure 4**, red).[42] Upon the addition of phenol (PhOH) under CO_2 saturation conditions, each complex shows an increase in current relative to aprotic conditions, consistent with the electrocatalytic response observed for **1** previously (**Figures 4, S14** and **S15**). Titrations of PhOH show that a plateau current is reached at 0.9 M PhOH for **2** with $E_{cat/2}$ = –2.33 V vs Fc^+/Fc and 0.5 M PhOH for **3** with $E_{cat/2}$ = –2.33 V vs Fc^+/Fc at 100 mV/s scan rate (**Figures S16** and **S17**).

In our previous study, we noted that **1** showed: (A) decreased current densities under increasing CO_2 concentrations due to the suppression of competitive HER activity, (B) no dependence on PhOH concentration, and (C) a first-order dependence on catalyst concentration.[41] For **2**, current saturation was observed above concentrations of 0.04 M CO_2 in

the presence of 1.0 M PhOH, and a first-order concentration dependence on PhOH was observed under CO_2 saturation conditions (**Figures S18-S19**). We again observed electrocatalytic current saturation above 0.04 M CO_2 for complex **3**; however, varied PhOH concentrations under saturated CO_2 give a slope of 0.15, suggesting a kinetically limiting effect in the overall mechanism (**Figures S20-S21**). These results indicate that a different mechanism is occurring in **2** and **3**, in comparison to **1**, which we hypothesize is the result of a fast proton shuttling mechanism for **2** and a slow one for **3**. Plots comparing the current response to the [catalyst] were linear for both **2** and **3**, suggesting the reaction is first order with respect to each, consistent with our prior study (**Figure S22-S23**).[41] Catalytic rate constants were determined for each complex utilizing variable scan rate experiments at 0.5 M PhOH for **3** and both 0.5 and 0.9 M PhOH for **2** by previously described methods.[43] At 0.5 M PhOH, **3** exhibits a $TOF_{max} = 436\pm1$ s^{-1}, while **2** exhibits $TOF_{max} = 303\pm1$ s^{-1}. At 1.0 M PhOH, **2** exhibits an increased $TOF_{max} = 587\pm1$ s^{-1} (**Figures S24-S26**). By treating the catalytic response observed for **1** with the same method for a 0.5 M concentration of PhOH, the TOF_{max} was determined to be 22 ± 1 s^{-1} (**Figure S27**). Kinetic isotope effects (k_H/k_D) were examined for both **2** and **3**, with both exhibiting a minimal isotope effect: **2** $k_H/k_D = 1.0$ and **3** $k_H/k_D = 1.7$. These results are in stark contrast to **1** which had a KIE of 4.8, suggesting that the pendent relays in **2** and **3** have modified the mechanism of proton transfer, which we interpret as a kinetic effect on the rates of Fe protonation and hydride transfer (**Figures S28** and **S29)**.
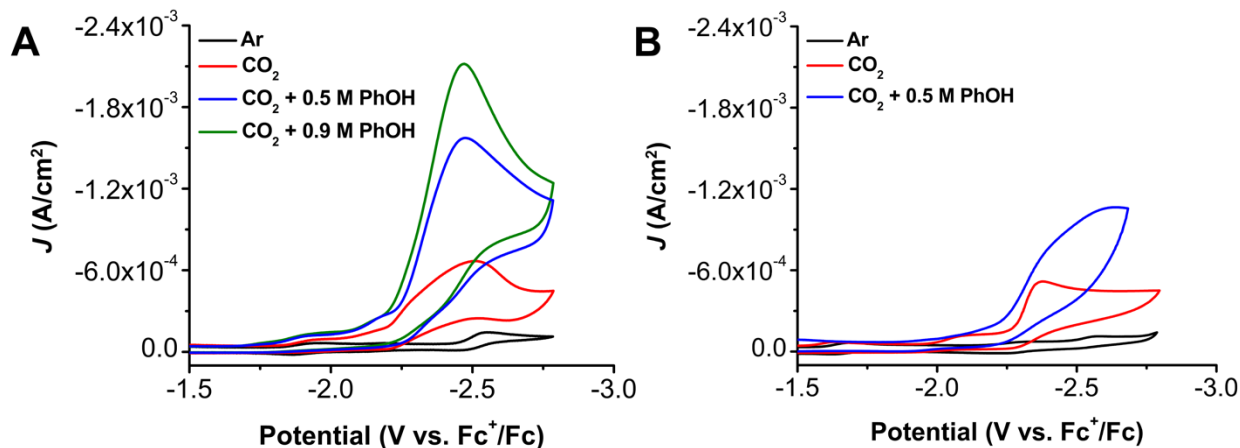
Figure 4. CVs of **(A) 2** and **(B) 3** under Ar (black) and CO_2 (red, blue, and green) saturation conditions. Blue and green traces are in the presence of PhOH added as a proton source. Working electrode is glassy carbon, counter electrode is a glassy carbon rod, AgCl/Ag pseudoreference electrode. Referenced to internal Cp_2^*Fe standard. 100 mV/s scan rate.

The catalytic efficiencies and selectivities of **2** and **3** for the reduction of CO_2 were determined by controlled potential electrolysis (CPE) experiments at the peak catalytic potentials for their respective PhOH saturation concentrations (**Table 1**). CPE at –2.50 V vs Fc^+/Fc with **2** and 0.9 M PhOH under CO_2 saturation conditions produced 85±2% HCO_2^- with the remainder of current going to H_2 (12±4%) and CO (5±1%) through 11.0 TON (22 electron equivalents passed per catalyst molecule, **Figure S30**). CPE at –2.60 V vs Fc^+/Fc with **3** and 0.5 M PhOH under CO_2 saturation conditions yielded 71±3% HCO_2^-, with the remainder of current going to H_2 (23±9%) and CO (0.8±0.1%) (**Figure S31**). Following these electrolysis experiments, the working electrode was rinsed with ethanol and allowed to air dry before a second electrolysis experiment was conducted where the putative molecular precatalyst was omitted under otherwise identical conditions of proton donor concentration and CO_2 saturation (**Figures S30** and **S31**, blue). The rinse test with both **2** and **3** indicated no HCO_2^- production (**Table 1**). Additional control experiments with no added catalyst material and a freshly polished electrode generated no HCO_2^- under either set of conditions (**Table 1**).

To examine HER activity in the absence of CO_2, CPE experiments were carried out with both **2** and **3** in the presence of 0.9 M and 0.5 M PhOH under an Ar atmosphere at –2.50 V and –2.60 V vs Fc^+/Fc, respectively (**Figure S32-33**). For **2**, 51±9% FE for H_2 was observed with no CO or

HCO_2^- detected after 9.5 TON. For **3**, 48±8% FE for H_2 was observed with no CO or HCO_2^- detected after 13 TON. A CPE experiment was also carried out with **3** with no PhOH added to probe whether H_2 could be generated from the pendent proton in each monomer at –2.71 V vs Fc^+/Fc (**Figure S34**). In this case, no H_2 was observed after eight electron equivalents of charge were passed.

Table 1. Summary of Controlled Potential Electrolysis Data.[a]

| Trial	Complex	TON	Formate[b] (HCO_2^-)	CO[b]	H_2[b]
1[c]	**2**	9.0	85±3	9±2	10±2
2[c]	**2**	11.0	84±1	5±1	12±4
3[c]	Rinse **2**	-	ND	6±2	32±4
4[c]	**-**	-	ND	ND	60±10
5[d]	**3**	9.4	70±8	2±1	28±4
6[d]	**3**	9.8	71±3	0.8±0.1	23±9
7[d]	Rinse **3**	-	ND	4±1	ND
8[d]	**-**	-	ND	1.0±0.5	17±7

Conditions were 0.1 M TBAPF$_6$/*N,N*-DMF supporting electrolyte with 0.5 M Fc as sacrificial oxidant. Working and counter electrodes were graphite rods, pseudoreference was Ag/AgCl. [b]FE. [c]0.9 M PhOH, –2.5 V vs Fc^+/Fc. [d]0.5 M PhOH, –2.6 V vs Fc^+/Fc.

To assess the proposed pendent proton relay mechanisms for **2** and **3**, CV experiments were repeated using 2,4,6-tri-*tert*-butyl-phenol (ΔpK_a^{DMSO} = 0.2[44], pK_a values are known scale well between DMSO and *N,N*-DMF[45]) as a sterically hindered proton source (**Figure S35**).[46] At concentrations of 2,4,6-tri-*tert*-butyl-phenol comparable to that of PhOH at saturation of the catalytic response, only **2** showed an increase in current relative to the background electrode current. This suggests that the pendent methoxy group in **2** is more efficient at relaying the proton donor to the active site than the hydroxy/phenolate moieties present in **3**.[32]

Discussion

In the case of both **2** and **3**, an enhanced TOF$_{max}$ in comparison to our original report with **1** is observed under saturation conditions. Only complex **2** shows increased selectivity for HCO_2^-, which suggests that under catalytic conditions, the production of H_2 is suppressed. We ascribe this in part to differences in the efficiency of the proton relay mechanism and to differences in the

effective pK_a of the protonated relay.[47] To boost a molecular electrocatalytic response, the forward reaction rate constant of proton transfer from exogenous proton source through the pendent relay to the active site must compare favorably to protonation directly at the active site by the exogenous proton source (**Figure 5**). We propose that the existence of the zwitterionic state of **3** in the secondary sphere is suggestive of possible deleterious effects on catalyst turnover due to the partial or complete deprotonation of the pendent –OH groups during the reaction. If deprotonation occurs during the catalytic turnover of **3**, non-covalent interactions with the sacrificial proton donor will be much stronger than for the neutral methoxy groups in complex **2** for purely electrostatic reasons, which could inhibit the catalytic response.[45, 48] Consistent with this interpretation, the experimental results with a sterically hindered proton source demonstrated catalytic current increases only for **2** (**Figure S35**). This suggests that for complex **2**, the outer-sphere pendent Lewis basic site is a more accessible site for protonation and can more efficiently shuttle protons to the metal center, empirically suggesting a difference in proton activity. While it cannot be discounted that the hydricity or pK_a values of the putative Fe hydride intermediates for **2** and **3** are different based on changes in the electronic structure in their respective protonated and reduced forms, there is no observed difference between their $E_{cat/2}$, suggesting that the catalytically competent iron hydride is of comparable hydricity.[47, 49]
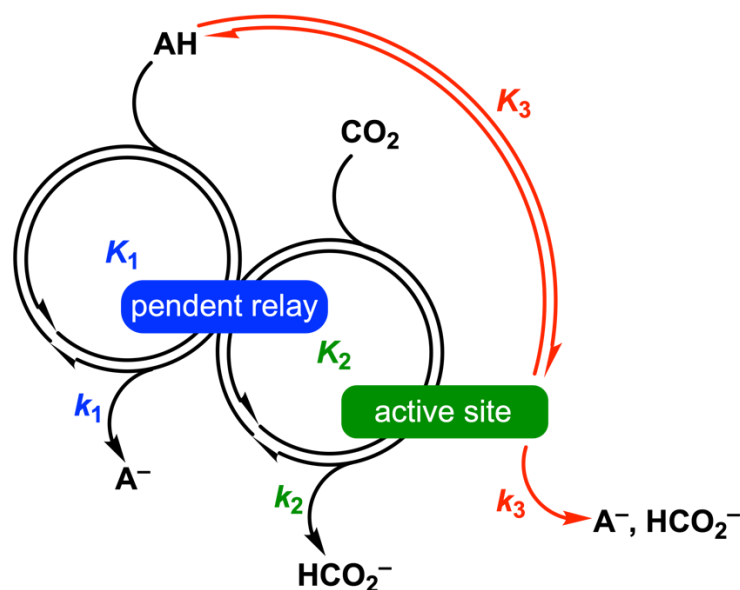
Figure 5. Summary of the basic relay mechanism of exogenous proton donor. For boosting effects to be observable in an electrocatalytic response, the forward reaction rate constants of the relay need to be competitive with the rate of direct protonation.[32] K are equilibria, and k are rate constants. In this case, the pendent relay would be either the methoxy ether (**2**) or the hydroxyl (**3**), and AH and A^- are PhOH and its conjugate base.

Conclusions

We have reported the synthesis, characterization, and reactivity for the electrocatalytic reduction of CO_2 to HCO_2^- of two new Fe(III) complexes with pendent proton relays. Enhancement of the catalytic rate constant is observed for both methyl-ether and hydroxy pendent functional groups. However, enhanced selectivity was only observed for the methyl-ether pendent functional group, suggesting that the strength of interaction between the external proton donor and the pendent relay site causes corresponding changes in the hydricity or pK_a of the putative intermediate hydride species. These results demonstrate that the pre-catalytic MS-EPT mechanism we observed in our original report is vital to the intrinsic catalytic properties and that the overall effect can be modulated through non-covalent secondary sphere interactions to optimize the catalytic response. This suggests that secondary sphere moieties which do not interact directly with substrate bound at the active site are a complementary way to modulate activity and selectivity in this class of catalyst.

Experimental and Methods

Materials and Methods

General. All chemicals and solvents (ACS or HPLC grade) were commercially available and used as received unless otherwise indicated. For all air-sensitive reactions and electrochemical experiments, solvents were obtained as anhydrous and air-free from a PPT Glass Contour Solvent Purification System. Gas cylinders were obtained from Praxair (Ar as 5.0; CO_2 as 4.0) and passed through molecular sieves prior to use. NMR spectra were obtained on a Varian 600 MHz or Bruker 800 MHz instrument and referenced to the residual solvent signal. Microwave reactions were carried out using an Anton-Parr Multiwave Pro SOLV, NXF-8 microwave reactor. Flash chromatography columns were run utilizing Teledyne ISCO CombiFlashRf+. UV-vis absorbance spectra were obtained on a Cary 60 from Agilent. GC experiments were performed using an Agilent 7890B Gas Chromatograph with an Agilent J&W Select Permanent Gases/CO_2 column and thermal conductivity detector; eluent retention times and product characterization were determined by standard injections. Formate was quantified by a previously reported NMR method.[50] HRMS data were obtained by the Mass Spectrometry Lab at the University of Illinois at Urbana-Champaign or on an Agilent 6545 Q-TOF LC/MS at UVA and elemental analyses were performed by Midwest Microlab. All synthetic procedures are summarized in **Scheme 1** and **Scheme 2** below.

Electrochemistry. All electroanalytical experiments were performed using a Metrohm Autolab PGSTAT302N or Biologic SP-50 potentiostats. Glassy carbon working (3 mm) and non-aqueous silver/silver chloride pseudoreference electrodes behind PTFE tips were obtained from CH Instruments. The pseudoreference electrodes were obtained by depositing chloride on bare silver wire in 10% HCl at oxidizing potentials and stored in a solution of 0.1 M tetrabutylammonium hexafluorophosphate (TBAPF$_6$) in *N,N*-dimethylformamide (DMF) prior to use. The counter electrode was a glassy carbon rod (Alfa Aesar, 99.95%, 3 mm diameter). All CV experiments

were performed in a modified scintillation vial (20 mL volume) as a single-chamber cell with a cap modified with ports for all electrodes and a sparging needle. Controlled potential electrolysis (CPE) experiments were performed in a H-cell with a porous glass frit separating the working and counter chambers. Prior to electrolysis, a CV of ferrocene was obtained to reference the cell. CPE experiments were run with graphite working and counter electrodes (Electron Microscopy Sciences, type A, 3 mm diameter) a custom silver/silver chloride pseudoreference electrode (BASi, non-aqueous reference electrode kit), and ports for head-space sampling and gas sparging via needles through septa. The working chamber was separated from the counter and pseudoreference electrodes utilizing a porous glass frit, and 0.05 M ferrocene was added to the counter chamber as a sacrificial reductant. TBAPF$_6$ was purified by recrystallization from ethanol and dried in a vacuum oven before being stored in a desiccator. All data were referenced to an internal decamethylferrocene (Cp$^*_2$Fe) standard (decamethylferricenium/decamethylferrocene reduction potential under stated conditions) which was subsequently corrected relative to the relative E$_{1/2}$ of ferrocene[51] unless otherwise specified.

Scheme 1 Synthesis of ^{me}crebpy[H$_2$].

^{me}crebpy(H)$_2$
60%
III

Fe(^{me}crebpy)Cl
70%
IV
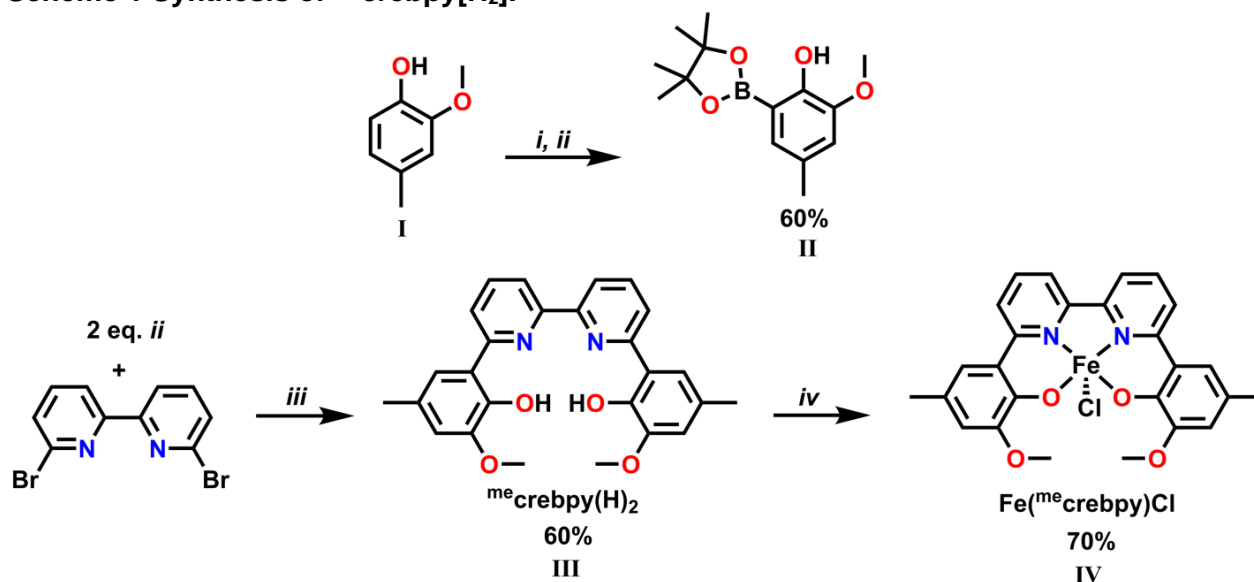
(*i*) 4,4,5,5-tetramethyl-1,3,2-dioxaborolane, RT, 10 m. (*ii*) 4,4,5,5-tetramethyl-2-(4,4,5,5-tetramethyl-1,3,2-dioxaborolan-2-yl)-1,3,2-dioxaborolane, 4-tert-butyl-2-(4-tert-butyl-2-pyridyl)pyridine, Ir[(cod)(OMe)]$_2$, cyclohexane, 90°C 21 h. (*iii*) Pd(PPh$_3$)$_4$, K$_3$PO$_4$, 1,4-dioxane, 130°C, 72 h. (*iv*) FeCl$_3$•6H$_2$O, NaOAc, EtOH, 78°C, 12 h.

**Synthesis of 2-methoxy-4-methyl-6-(4,4,5,5-tetramethyl-1,3,2-dioxaborolan-2-yl)phenol[52],
II.** In a glovebox, 2-methoxy-4-methyl-phenol (2.5 mL, 19.7 mmol) and 4,4,5,5-tetramethyl-1,3,2-dioxaborolane (2.5 mL, 21.7 mmol) were combined and stirred for 10 m in a 250 mL pressure flask. Vigorous effervescence was observed. After this time, 4,4,5,5-tetramethyl-2-(4,4,5,5-tetramethyl-1,3,2-dioxaborolan-2-yl)-1,3,2-dioxaborolane (3.51 g, 13.8 mmol), 4-tert-butyl-2-(4-tert-butyl-2-pyridyl)pyridine (0.318 g, 6 mol %), Ir[(cod)(OMe)]$_2$ (0.392 g, 3 mol %), and 100 mL of dry cyclohexane were added. The flask was capped, and heated to 90 °C for 21 h. After this time, the flask was allowed to cool to room temperature, 10 g of silica gel was added, and solvent was removed to dryness under reduced pressure. A silica gel column was run using a Combiflash purification system (ramp 0 to 10 % EtOAc/Hexanes) and the fraction which eluted after the starting material was isolated (very little UV-Vis absorbance is observed for the product). Solvent was removed to yield 2.52 g of a pale-yellow solid. Yield: 48.4%. Characterization was consistent with prior reports.[52]

^{me}crebpy(H)$_2$, III. A 500 mL pressure flask with stir bar was charged with 6,6′-dibromobipyridine (0.7 g, 2.23 mmol), K$_3$PO$_4$ (2.56 g, 12 mmol), 2-methoxy-4-methyl-6-(4,4,5,5-tetramethyl-1,3,2-dioxaborolan-2-yl)phenol (1.77 g, 6.69 mmol), Pd(PPh$_3$)$_4$ (0.260 g, 0.22 mmol), and dioxane (250 mL). After this time, the mixture was cooled to RT, diluted with brine (250 mL), and extracted with toluene (6x50 ml) and CH$_2$Cl$_2$ (6x50 mL). The organic layers were combined and dried with MgSO$_4$, filtered, and dried under reduced vacuum. The yellow product elutes from a CH$_2$Cl$_2$/MeOH ramp of 0-5 % MeOH using a Combiflash purification system. Recrystallization of the product fraction from CH$_2$Cl$_2$/hexanes yields pure product. Yield: 0.430 g, 45%. ESI-MS (*m/z*) [M+H]$^+$: Calc'd 429.181 Found: 429.181. CHN analysis: Theory (CHN): C: 72.88, H: 5.65, N: 6.54. Found: C: 72.59, H: 5.53, N: 6.32. ^{1}H NMR (DMSO-d$_7$, 600 MHz): δ (ppm) 2.34 (s, 6H), 3.82 (s, 6H), 6.92 (s, 2H), 7.50 (s, 2H), 8.13 (d, 2H), 8.21 (t, 2H), 8.29 (d, 2H), 13.18 (s, 2H). ^{13}C{^{1}H} NMR (DMSO-d$_7$, 600 MHz): δ (ppm) 20.82, 55.79, 114.71, 119.11, 119.18, 119.25, 121.60, 127.17, 139.59, 146.37, 148.50, 151.86, 157.10.

Synthesis of Fe(^(me)crebpy)Cl, 2, IV. Ferric chloride hexahydrate (Fe(Cl)$_3$•6H$_2$O, 0.088 g, 0.33 mmol), sodium acetate (NaOAc, 0.052 g, 0.64 mmol), and 6,6'-([2,2'-bipyridine]-6,6'-diyl)bis(2-methoxy-4-methylphenol) (0.133 g, 0.310 mmol) were combined in a 100 mL round-bottom flask (RBF) equipped with stir bar. EtOH (20 mL) was added to the solids and the solution was brought to reflux overnight for 16 h. The resulting suspension was removed from heat, and the remaining dark red-black solid was collected by vacuum filtration, washed with water (3x10 mL) and diethyl ether (3x5 mL). Crystals suitable for X-ray diffraction were grown by slow cooling a boiling saturated acetonitrile solution. Yield: 0.120 g, 74.1%. UV-vis in *N,N*- DMF: λ_{max}: 354 nm (ε: 28000 M^{-1}cm^{-1}) and 473 nm (ε: 5300 M^{-1}cm^{-1}). CHN Analysis: Theory (FeC$_{26}$H$_{22}$N$_2$O$_4$•0.5H$_2$O): C: 60.31, H: 4.28, N: 5.41. Found: C: 59.15, H: 4.21, N: 5.09. ESI-MS (*m/z*) [M+Na]$^+$: Calc'd 540.052 Found: 540.045. Magnetic Moment: 5.9±0.1 BM.

Zn(^(me)crebpy). 6,6'-([2,2'-bipyridine]-6,6'-diyl)bis(2-methoxy-4-methylphenol) (0.61 g, 0.142 mmol), sodium acetate (23.9 mg, 0.29 mmol), zinc dichloride (0.020 g, 0.149 mmol), and absolute ethanol (20 mL) were combined in a 100 mL RBF equipped with stir bar and condenser. The mixture was brought to reflux (78 °C) overnight (16 h). After this time, a yellow-orange precipitate formed and was collected via vacuum filtration, washed with DI water (1x5 mL) and diethyl ether (1x5 mL). Yield: 21 mg, 30%. CHN analysis Theory (ZnC$_{26}$H$_{22}$N$_2$O$_4$•3H$_2$O): C: 57.21, H: 5.17, N: 5.13. Found: C: 56.90, H: 4.26, N: 5.05. ^{1}H NMR (DMSO-d$_7$, 600 MHz): δ (ppm) 2.25 (s, 6H), 3.76 (s, 6H), 6.65 (s, 2H), 7.10 (s, 2H), 8.01 (d, 2H), 8.13 (t, 2H), 8.31 (d, 2H). ^{13}C{^{1}H} NMR (DMSO-d$_6$, 600 MHz): (**L^1**) δ (ppm) 21.04, 55.10, 112.39, 117.82, 120.17, 123.24, 140.03, 147.76, 152.31, 156.88, 159.23.

SCHEME 2. Synthesis for Fe(^{tbu}catbpy).
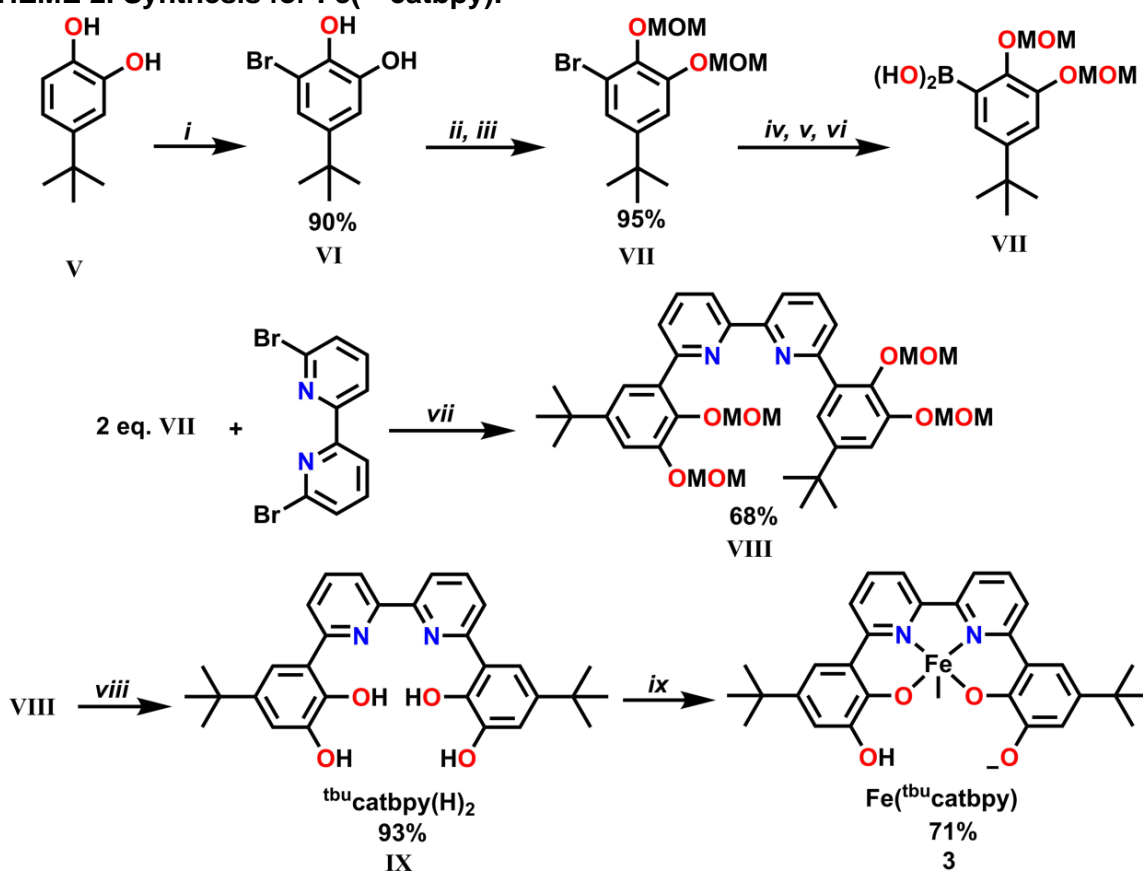
(*i*) NBS, *N,N*-DMF, N$_2$, room temperature, 2 h. (*ii*) DIPEA, N$_2$, CH$_2$Cl$_2$. (*iii*) MOMCl, 0°C→RT, 5 h. (*iv*) ^{n}BuLi, -78°C→RT, 2 h. (*v*) B(OMe)$_3$, -78°C→RT, 16 h. (*vi*) 2 M HCl. (*vii*) Pd(PPh$_3$)$_4$, Na$_2$CO$_3$, toluene, MeOH, H$_2$O, 280 W microwave irradiation, 5 h. (*viii*) HCl(g), EtOAc. (*ix*) FeCl$_3$•6H$_2$O, NaOAc, EtOH, 78°C, 3 h.

3-bromo-5-*tert*-butyl-benzene-1,2-diol[53]**, VI.** 4-*tert*-butyl catechol **(V)** (10.0 g, 0.0602 mol) was dissolved in *N,N*-DMF (25 mL) in a 200 mL Schlenk RBF with a stir bar under nitrogen. A 2.0 M solution of *N*-bromosuccinimide in *N,N*-DMF (30.0 mL, 0.0662 mol) was added to the solution dropwise via syringe with vigorous stirring. After 2 h the solution was diluted with 100 mL ethyl acetate, washed with water (3x50 mL), and washed with brine (3x50 mL). The organic fraction was collected, dried over MgSO$_4$, filtered, and the solvent was removed under reduced pressure to yield a dark red oil. Note: the oil can be used without further purification, however, sublimation of the oil produces white X-ray quality crystals of analytical purity. (Yield: 13.2 g, 89.5%). ES-MS (*m/z*) [M]$^+$: Calc'd 244.0099 Found: 244.0098. ^{1}H NMR (CDCl$_3$, 600 MHz): δ (ppm) 1.26 (s, 9H),

6.92 (d, 1H), 6.99 (d, 1H). $^{13}C\{^1H\}$ NMR (CDCl$_3$, 600 MHz): (**L^1**) δ (ppm) 31.43, 34.55, 109.23, 112.69, 120.16, 137.98, 144.08, 145.78.

1-bromo-5-*tert*-butyl-2,3-bis(methoxymethoxy)benzene, VII. Dry dichloromethane (50 mL) was dispensed in an oven-dried RBF (250 mL). To this flask, an oven-dried stir bar, 3-bromo-5-*tert*-butyl-benzene-1,2-diol (8.67 g, 35.4 mmol) were added. The headspace was flushed with nitrogen and diisopropylethylamine (21.6 mL, 124.0 mmol) was added. A color change from brown to maroon was observed. The RBF was cooled to 0 °C using an ice bath. Methoxymethylchloride (8.1 mL, 110 mmol) was added dropwise with vigorous stirring. After the addition, the ice bath was removed and the solution was allowed to stir for 5 h. The reaction was quenched with aqueous NH$_4$OH (2 N, 120 mL), the organic layer was separated, and the aqueous layer was extracted using diethyl ether (3x50 mL). The organic fractions were combined, washed with brine (3x50 mL), dried over MgSO$_4$, and condensed in vacuo to yield a red oil. Yield 11.2 g, 94.9 %. EI-MS (*m/z*) [M]$^+$: Calc'd 332. Found: 332. ^1H NMR (CDCl$_3$, 600 MHz): δ (ppm) 1.28 (s, 9H), 3.51 (s, 3H), 3.67 (s, 3H), 5.16 (s, 2H), 5.18 ppm (s, 2H) 7.10 (d, 1H), 7.21 (d, 1H). $^{13}C\{^1H\}$ NMR (CD$_2$Cl$_2$, 600 MHz): δ (ppm) 31.39, 34.91, 56.52, 58.08, 95.83, 98.97, 114.07, 117.42, 123.81, 142.04, 148.99, 150.64.

bis(MOM)catbpy, VIII. A 500 mL Schlenk flask with stir bar was charged with 1-bromo-5-*tert*-butyl-2,3-bis(methoxymethoxy)benzene (11.2 g, 33.6 mmol) and dry diethyl ether (100 mL). The resulting solution was cooled to -78°C under N$_2$. *n*-Butyllithium (1.6 M in hexanes) was added dropwise via syringe (23.1 mL, 36.9 mmol) still under N$_2$, after which the solution was allowed to warm to room temperature with vigorous stirring. At this point the reaction mixture was a brown suspension. After two hours the solution was returned to -78°C. Trimethylborate was added rapidly by syringe (3.95 mL, 35.3 mmol) with vigorous stirring and left for 10 minutes before the cold bath was removed and the mixture left overnight under N$_2$ (16 h). After this time the reaction was quenched with deionized water (50 mL) and opened to air. The suspension was extracted and the aqueous and organic layers separated. The aqueous layer was carefully neutralized to

pH = 7 with ~0.1 M HCl, washed with diethyl ether (3x50 mL), and all organic fractions were combined. The combined layers were then washed with brine (3x50 mL). The resulting solution was dried with $MgSO_4$ for 10 minutes, before the mixture was filtered to remove solid and the solvent was removed under reduced pressure. The resulting dark orange oil was used as isolated without further purification.

A microwave-assisted Suzuki-Miyaura coupling reaction was performed with 6,6′-dibromo-2,2′-bipyridine and the crude boronic acid generated above using an Anton Paar Multiwave Pro equipped with Rotor 8NXF100. Two PTFE reaction tubes were equipped with a magnetic stir bar and charged with 6,6′-dibromo-2,2′-bipyridine (1.0 g, 3.2 mmol) and Na_2CO_3 (2.0 g, 38 mmol), each. Deionized water and methanol were degassed with Ar. The loaded PTFE tubes, solvents, and crude boronic acid were pumped into a N_2 glovebox. $Pd(PPh_3)_4$ (0.18 g, 0.16 mmol) was added to each tube. The boronic acid was added to this suspension by diluting in toluene (20 mL total volume) and splitting this stock solution equally between the two PTFE vessels. Methanol (10 mL), deionized water (10 mL), and toluene (30 mL) were added to the vessels. The vessels were sealed, and loaded into the microwave. The power was ramped to 280 W for 10 m, and then held at this value for 5 h. After cooling to room temperature, the tubes were combined, and the organic and aqueous layers were separated. The aqueous layer was extracted with CH_2Cl_2 (3 x 50 mL) and all organic fractions were combined, dried with $MgSO_4$, filtered to remove solids, and condensed under vacuum to yield a crude red oil. This oil was left overnight at room temperature, and an off-white crystalline solid formed overnight. This solid was collected, and washed with hexanes. Upon combination of the hexanes wash and the initial fraction, more crystalline material was produced. Characterization of each fraction was consistent with the desired product. Yield 2.85 g, 67.7 %. EI-MS (*m/z*) [M-H]+: Calc'd 661.3489. Found: 661.3486. Theory (CHN): C: 69.07, H: 68.83, N: 7.32. Found: C: 68.83, H: 7.24, N: 4.02. ^{1}H NMR ($CDCl_3$, 600 MHz): δ (ppm) 1.39 (s, 18H), 3.12 (s, 6H), 3.56 (s, 6H), 4.96 (s, 4H), 5.27 ppm (s, 4H), 7.27 (d, 2H), 7.55 (d, 2H)), 7.81-

7.88 (m, 4H), 8.53 (d, 2H). $^{13}C\{^1H\}$ NMR (CDCl$_3$, 600 MHz): δ (ppm) 31.60, 34.91, 56.45, 57.23, 95.89, 99.37, 115.17, 119.45, 121.54, 125.57, 134.95, 136.76, 142.57, 147.85, 150.04, 155.96.

^{tbu}catbpy, IX. 6,6'-bis(5-(tert-butyl)-2,3-bis(methoxymethoxy)phenyl)-2,2'-bipyridine (2.50 g, 3.78 mmol) was dissolved in minimal EtOAc (~100 mL) in a 250 mL RBF equipped with stir bar. Excess anhydrous HCl was generated by adding concentrated H$_2$SO$_4$ dropwise to solid NaCl in an airtight vessel that vented through the EtOAc solution via PTFE cannula transfer. Excess HCl was quenched by venting through an outlet flask containing saturated aq. NaHCO$_3$. The flask containing EtOAc was sealed, and left to stir overnight. During the ~9 h of stirring, the EtOAc solution changed from colorless to yellow, and a solid precipitated from solution. After purging the EtOAc solution with N$_2$, saturated aq. NaHCO$_3$ was added to ensure neutralization. The resultant solid was collected via vacuum filtration, washed with water, and triturated with CHCl$_3$ to yield the desired product as an orange powder. Yield: 1.71 g, 93.3 %. EI-MS (*m/z*) [M-H]$^+$: Calc'd 485.2440. Found: 485.2435. CHN analysis: Theory (C$_{30}$H$_{32}$N$_2$O$_4$•0.8CHCl$_3$): C: 63.77, H: 5.70, N: 4.83. Found: C: 63.84, H: 5.69, N: 4.69. ^1H NMR (DMSO-d$_7$, 600 MHz): δ (ppm) 1.31 (s, 18H), 6.89 (s, 2H), 7.49 (s, 2H), 8.04-8.20 (m, 4H), 8.45 (s, 2H). $^{13}C\{^1H\}$ NMR (DMSO-d$_7$, 600 MHz): δ (ppm) 31.33, 33.94, 113.88, 114.71, 118.78, 118.92, 121.44, 139.64, 141.06, 145.01, 145.86, 151.91, 157.70.

Fe(^{tbu}catbpy), 3. 6,6'-([2,2'-bipyridine]-6,6'-diyl)bis(4-(*tert*-butyl)benzene-1,2-diol) (0.150 g, 0.310 mmol), NaOAc (52.1 mg, 0.63 mmol), Fe(Cl)$_3$•6H$_2$O (0.088 g, 0.33 mmol), and absolute ethanol (20 mL) were combined in a 100 mL RBF equipped with stir bar and condenser. The mixture was brought to reflux (78 °C) overnight (16 h). The resulting black suspension was removed from heat and the volume reduced to ~10 mL *in vacuo* before DI H$_2$O (5 mL) was added, inducing the formation of a black precipitate. The solid was collected by vacuum filtration and washed with H$_2$O (3 x 5 mL) and Et$_2$O (3x5 mL). Yield: 0.119 g, 71%. UV-vis in *N,N-* DMF: λ$_{max}$: 290, 345, and 560 nm. ε: 31000, 20000, and 3700 M^{-1} cm^{-1}, respectively EI-MS (*m/z*) [M-H]$^+$: Calc'd 535.1555.

Found: 535.1553. CHNCl analysis: None. Theory (FeC$_{30}$H$_{29}$N$_2$O$_4$•2H$_2$O): C: 62.84, H: 5.80, N: 4.89, Cl: None. Found: C: 63.08, H: 5.26, N: 4.92, Cl: None. Magnetic Moment: 6.1±0.1 BM.

Synthesis of Zn(^{tbu}catbpy). 6,6'-([2,2'-bipyridine]-6,6'-diyl)bis(4-(*tert*-butyl)benzene-1,2-diol) (0.052 g, 0.108 mmol), sodium acetate (18.1 mg, 0.22 mmol), zinc dichloride (0.015 g, 0.11 mmol), and absolute ethanol (20 mL) were combined in a 100 mL RBF equipped with stir bar and condenser. The mixture was brought to reflux (78 °C) overnight (16 h). After this time, a yellow-orange precipitate formed and was collected via vacuum filtration, washed with DI water (1x5 ml) and diethyl ether (1x5mL). Yield: 39 mg, 68%. CHN analysis Theory: C: 65.76, H: 5.52, N: 5.11. Found: C: 65.20, H: 5.29, N: 4.90. ^{1}H NMR (DMSO-d$_7$, 600 MHz): δ (ppm) 1.26 (s, 18H), 6.80 (s, 2H), 7.02 (s, 2H)), 8.05 (d, 2H), 8.15 (t, 2H), 8.34 (d, 2H). ^{13}C{^{1}H} NMR (DMSO-d$_7$, 600 MHz): δ (ppm) 31.47, 33.75, 110.26, 114.18, 116.55, 118.00, 135.09, 140.47, 147.74, 149.71, 154.32, 159.82.

Associated Content

Supporting Information document available online.

Author Information

Corresponding Author

*machan@virginia.edu

ORCID: Charles W. Machan: 0000-0002-5182-1138

Notes

The authors declare no competing interest.

Acknowledgements

Bibliography

1.   Senftle, T. P.; Carter, E. A. The Holy Grail: Chemistry Enabling an Economically Viable CO2 Capture, Utilization, and Storage Strategy. *Acc. Chem. Res.* **2017,** 50 (3), 472-475 DOI: 10.1021/acs.accounts.6b00479.

2.   De Luna, P.; Hahn, C.; Higgins, D.; Jaffer, S. A.; Jaramillo, T. F.; Sargent, E. H. What would it take for renewably powered electrosynthesis to displace petrochemical processes? *Science* **2019,** 364 (6438), eaav3506 DOI: 10.1126/science.aav3506.

3.   Francke, R.; Schille, B.; Roemelt, M. Homogeneously Catalyzed Electroreduction of Carbon Dioxide—Methods, Mechanisms, and Catalysts. *Chem. Rev.* **2018,** 118 (9), 4631-4701 DOI: 10.1021/acs.chemrev.7b00459.

4.   Witt, S. E.; White, T. A.; Li, Z.; Dunbar, K. R.; Turro, C. Cationic dirhodium(ii,ii) complexes for the electrocatalytic reduction of CO2 to HCOOH. *Chem. Commun.* **2016,** 52 (82), 12175-12178 DOI: 10.1039/C6CC03253B.

5.   Roy, S.; Sharma, B.; Pécaut, J.; Simon, P.; Fontecave, M.; Tran, P. D.; Derat, E.; Artero, V. Molecular cobalt complexes with pendant amines for selective electrocatalytic reduction of carbon dioxide to formic acid. *J. Am. Chem. Soc* **2017,** 139 (10), 3685-3696.

6.   Clarke, H. T.; Gillespie, H. B.; Weisshaus, S. Z. The Action of Formaldehyde on Amines and Amino Acids1. *J. Am. Chem. Soc.* **1933,** 55 (11), 4571-4587 DOI: 10.1021/ja01338a041.

7.   Rice, C.; Ha, S.; Masel, R.; Waszczuk, P.; Wieckowski, A.; Barnard, T. Direct formic acid fuel cells. *J. Power Sources* **2002,** 111 (1), 83-89.

8.   Hull, J. F.; Himeda, Y.; Wang, W.-H.; Hashiguchi, B.; Periana, R.; Szalda, D. J.; Muckerman, J. T.; Fujita, E. Reversible hydrogen storage using CO 2 and a proton-switchable iridium catalyst in aqueous media under mild temperatures and pressures. *Nat. Chem.* **2012,** 4 (5), 383.

9.   Nichols, A. W.; Chatterjee, S.; Sabat, M.; Machan, C. W. Electrocatalytic Reduction of CO2 to Formate by an Iron Schiff Base Complex. *Inorg. Chem.* **2018,** 57 (4), 2111-2121 DOI: 10.1021/acs.inorgchem.7b02955.

10.   Lieske, L. E.; Hooe, S. L.; Nichols, A. W.; Machan, C. W. Electrocatalytic reduction of dioxygen by Mn(iii) meso-tetra(N-methylpyridinium-4-yl)porphyrin in universal buffer. *Dalton Trans.* **2019,** 48, 8633-8641 DOI: 10.1039/C9DT01436E.

11.   Hooe, S. L.; Machan, C. W. Dioxygen Reduction to Hydrogen Peroxide by a Molecular Mn Complex: Mechanistic Divergence between Homogeneous and Heterogeneous Reductants. *J. Am. Chem. Soc.* **2019,** 141 (10), 4379-4387 DOI: 10.1021/jacs.8b13373.

12.   Huynh, M. H. V.; Meyer, T. J. Proton-Coupled Electron Transfer. *Chem. Rev.* **2007,** 107 (11), 5004-5064 DOI: 10.1021/cr0500030.

13.   Solis, B. H.; Yu, Y.; Hammes-Schiffer, S. Effects of Ligand Modification and Protonation on Metal Oxime Hydrogen Evolution Electrocatalysts. *Inorg. Chem.* **2013,** 52 (12), 6994-6999 DOI: 10.1021/ic400490y.

14.   Kaeffer, N.; Chavarot-Kerlidou, M.; Artero, V. Hydrogen Evolution Catalyzed by Cobalt Diimine-Dioxime Complexes. *Acc. Chem. Res.* **2015,** 48 (5), 1286-1295 DOI: 10.1021/acs.accounts.5b00058.
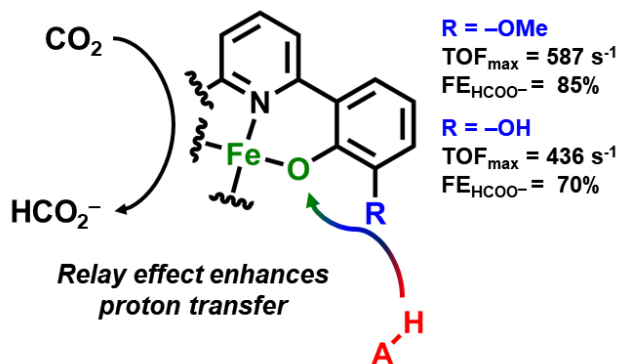
15.   Downes, C. A.; Yoo, J. W.; Orchanian, N. M.; Haiges, R.; Marinescu, S. C. H2 evolution by a cobalt selenolate electrocatalyst and related mechanistic studies. *Chem. Commun.* **2017,** 53 (53), 7306-7309 DOI: 10.1039/C7CC02473H.

16.   Zarkadoulas, A.; Field, M. J.; Artero, V.; Mitsopoulou, C. A. Proton-Reduction Reaction Catalyzed by Homoleptic Nickel-bis-1,2-dithiolate Complexes: Experimental and Theoretical Mechanistic Investigations. *ChemCatChem* **2017,** 9 (12), 2308-2317 DOI: 10.1002/cctc.201601399.

17.   Chen, J.; Sit, P. H.-L. Density Functional Theory and Car–Parrinello Molecular Dynamics Study of the Hydrogen-Producing Mechanism of the Co (dmgBF2) 2 and Co (dmgH) 2 Cobaloxime Complexes in Acetonitrile–Water Solvent. *J. Phys. Chem. A* **2017,** 121 (18), 3515-3525.

18.   McEvoy, J. P.; Brudvig, G. W. Water-splitting chemistry of photosystem II. *Chem. Rev.* **2006,** 106 (11), 4455-4483.

19.   Manner, V. W.; DiPasquale, A. G.; Mayer, J. M. Facile Concerted Proton−Electron Transfers in a Ruthenium Terpyridine-4′-Carboxylate Complex with a Long Distance Between the Redox and Basic Sites. *J. Am. Chem. Soc.* **2008,** 130 (23), 7210-7211.

20.   Warren, J. J.; Tronic, T. A.; Mayer, J. M. Thermochemistry of proton-coupled electron transfer reagents and its implications. *Chem. Rev.* **2010,** 110 (12), 6961-7001 DOI: 10.1021/cr100085k.

21.   Fecenko, C. J.; Thorp, H. H.; Meyer, T. J. The Role of Free Energy Change in Coupled Electron−Proton Transfer. *J. Am. Chem. Soc.* **2007,** 129 (49), 15098-15099 DOI: 10.1021/ja072558d.

22.   Ngo, K. T.; McKinnon, M.; Mahanti, B.; Narayanan, R.; Grills, D. C.; Ertem, M. Z.; Rochford, J. Turning on the Protonation-First Pathway for Electrocatalytic CO2 Reduction by Manganese Bipyridyl Tricarbonyl Complexes. *J. Am. Chem. Soc.* **2017,** 139 (7), 2604-2618 DOI: 10.1021/jacs.6b08776.

23.   Costentin, C.; Drouet, S.; Robert, M.; Savéant, J.-M. A Local Proton Source Enhances CO2 Electroreduction to CO by a Molecular Fe Catalyst. *Science* **2012,** 338 (6103), 90–94 DOI: 10.1126/science.1224581.

24.   Roy, S.; Sharma, B.; Pécaut, J.; Simon, P.; Fontecave, M.; Tran, P. D.; Derat, E.; Artero, V. Molecular Cobalt Complexes with Pendant Amines for Selective Electrocatalytic Reduction of Carbon Dioxide to Formic Acid. *J. Am. Chem. Soc.* **2017,** 139 (10), 3685-3696 DOI: 10.1021/jacs.6b11474.

25.   Curtis, C. J.; Miedaner, A.; Ciancanelli, R.; Ellis, W. W.; Noll, B. C.; Rakowski DuBois, M.; DuBois, D. L. [Ni (Et2PCH2NMeCH2PEt2) 2] 2+ as a functional model for hydrogenases. *Inorg. Chem.* **2003,** 42 (1), 216-227.

26.   Henry, R. M.; Shoemaker, R. K.; DuBois, D. L.; DuBois, M. R. Pendant bases as proton relays in iron hydride and dihydrogen complexes. *J. Am. Chem. Soc.* **2006,** 128 (9), 3002-3010.

27.   Fraze, K.; Wilson, A. D.; Appel, A. M.; Rakowski DuBois, M.; DuBois, D. L. Thermodynamic Properties of the Ni− H Bond in Complexes of the Type [HNi (P2RN2R ') 2](BF4) and Evaluation of Factors That Control Catalytic Activity for Hydrogen Oxidation/Production. *Organometallics* **2007,** 26 (16), 3918-3924.

28.   Collman, J. P.; Boulatov, R.; Sunderland, C. J.; Fu, L. Functional analogues of cytochrome c oxidase, myoglobin, and hemoglobin. *Chem. Rev.* **2004,** 104 (2), 561-588.

29.   Collman, J. P. Synthetic models for the oxygen-binding hemoproteins. *Acc. Chem. Res.* **1977,** 10 (7), 265-272.

30.   Elwell, C. E.; Gagnon, N. L.; Neisen, B. D.; Dhar, D.; Spaeth, A. D.; Yee, G. M.; Tolman, W. B. Copper–Oxygen Complexes Revisited: Structures, Spectroscopy, and Reactivity. *Chem. Rev.* **2017,** 117 (3), 2059-2107 DOI: 10.1021/acs.chemrev.6b00636.

31.   Lewis, E. A.; Tolman, W. B. Reactivity of dioxygen− copper systems. *Chem. Rev.* **2004,** 104 (2), 1047-1076.

32.   Savéant, J.-M. Proton Relays in Molecular Catalysis of Electrochemical Reactions: Origin and Limitations of the Boosting Effect. *Angew. Chem., Int. Ed.* **2019,** 58 (7), 2125-2128 DOI: 10.1002/anie.201812375.

33.   Azcarate, I.; Costentin, C.; Robert, M.; Saveant, J.-M. Through-Space Charge Interaction Substituent Effects in Molecular Catalysis Leading to the Design of the Most Efficient Catalyst of CO2-to-CO Electrochemical Conversion. *J. Am. Chem. Soc.* **2016,** 138 (51), 16639-16644 DOI: 10.1021/jacs.6b07014.

34.   Costentin, C.; Passard, G.; Robert, M.; Savéant, J.-M. Pendant Acid–Base Groups in Molecular Catalysts: H-Bond Promoters or Proton Relays? Mechanisms of the Conversion of CO2 to CO by Electrogenerated Iron(0)Porphyrins Bearing Prepositioned Phenol Functionalities. *J. Am. Chem. Soc.* **2014,** 136 (33), 11821-11829 DOI: 10.1021/ja506193v.

35.   Jiang, C.; Nichols, A. W.; Machan, C. W. A look at periodic trends in d-block molecular electrocatalysts for CO2 reduction. *Dalton Trans.* **2019**, DOI: 10.1039/C9DT00491B.

36.   Costentin, C.; Passard, G.; Robert, M.; Saveant, J.-M. Ultraefficient homogeneous catalyst for the CO2-to-CO electrochemical conversion. *Proc. Natl. Acad. Sci.* **2014,** 111 (42), 14990-14994 DOI: 10.1073/pnas.1416697111.

37.   Nichols, A. W.; Machan, C. W. Secondary-Sphere Effects in Molecular Electrocatalytic CO2 Reduction. *Front. Chem.* **2019,** 7, https://doi.org/10.3389/fchem.2019.00397.

38.   Kadish, K. M.; Larson, G. A study of the redox potentials and electron transfer rates of several naturally occurring and synthetic iron porphyrins in DMF. *Bioinorg. Chem.* **1977,** 7 (2), 95-105 DOI: https://doi.org/10.1016/S0006-3061(00)80060-5.

39.   Savéant, J.-M. *Elements of molecular and biomolecular electrochemistry: an electrochemical approach to electron transfer chemistry*. John Wiley & Sons: 2006; Vol. 13.

40.   Bard, A. J.; Faulkner, L. R. *Electrochemical Methods: Fundamentals and Applications*. 2nd ed.; John Wiley & Sons, Inc.: Hoboken, NJ, 2001.

41.   Nichols, A. W., Chatterjee, S., Sabat, M., Machan, C. W. Electrocatalytic Reduction of CO2 to Formic Acid by an Iron Schiff Base Complex. *Inorg. Chem.* **2018**, DOI: ic-2017-02955r.

42.   Appel, A. M.; Helm, M. L. Determining the Overpotential for a Molecular Electrocatalyst. *ACS Catal.* **2014,** 4 (2), 630-633 DOI: 10.1021/cs401013v.

43.   Franco, F.; Pinto, M. F.; Royo, B.; Lloret-Fillol, J. A Highly Active N-Heterocyclic Carbene Manganese(I) Complex for Selective Electrocatalytic CO_2 Reduction to CO. *Angew. Chem. Int. Edit.* **2018,** 57 (17), 4603-4606 DOI: 10.1002/anie.201800705.

44.   Bordwell, F. G.; Cheng, J. Substituent effects on the stabilities of phenoxyl radicals and the acidities of phenoxyl radical cations. *J. Am. Chem. Soc.* **1991,** 113 (5), 1736-1743 DOI: 10.1021/ja00005a042.

45.   Clare, B.; Cook, D.; Ko, E.; Mac, Y.; Parker, A. Solvation of Ions. IX. 1 The Effect of Anion Solvation on Acid Dissociation Constants in Methanol, Water, Dimethylformamide, and Dimethyl Sulfoxide. *J. Am. Chem. Soc.* **1966,** 88 (9), 1911-1916.

46.   Machan, C. W.; Yin, J.; Chabolla, S. A.; Gilson, M. K.; Kubiak, C. P. Improving the Efficiency and Activity of Electrocatalysts for the Reduction of CO_2 through Supramolecular Assembly with Amino Acid-Modified Ligands. *J. Am. Chem. Soc.* **2016,** 138 (26), 8184-8193 DOI: 10.1021/jacs.6b03774.

47.   Waldie, K. M.; Ostericher, A. L.; Reineke, M. H.; Sasayama, A. F.; Kubiak, C. P. Hydricity of Transition-Metal Hydrides: Thermodynamic Considerations for CO_2 Reduction. *ACS Catal.* **2018,** 8 (2), 1313-1324 DOI: 10.1021/acscatal.7b03396.

48.   Sinha, S.; Warren, J. J. Unexpected Solvent Effect in Electrocatalytic CO_2 to CO Conversion Revealed Using Asymmetric Metalloporphyrins. *Inorg. Chem.* **2018,** 57 (20), 12650-12656 DOI: 10.1021/acs.inorgchem.8b01814.

49.   Wiedner, E. S.; Chambers, M. B.; Pitman, C. L.; Bullock, R. M.; Miller, A. J. M.; Appel, A. M. Thermodynamic Hydricity of Transition Metal Hydrides. *Chemical Reviews* **2016,** 116 (15), 8655-8692 DOI: 10.1021/acs.chemrev.6b00168.

50.   Nichols, A. W.; Chatterjee, S.; Sabat, M.; Machan, C. W. Electrocatalytic Reduction of CO_2 to Formate by an Iron Schiff Base Complex. *Inorganic Chemistry* **2018,** 57 (4), 2111-2121 DOI: 10.1021/acs.inorgchem.7b02955.

51.   Noviandri, I.; Brown, K. N.; Fleming, D. S.; Gulyas, P. T.; Lay, P. A.; Masters, A. F.; Phillips, L. The Decamethylferrocenium/Decamethylferrocene Redox Couple: A Superior Redox Standard to the Ferrocenium/Ferrocene Redox Couple for Studying Solvent Effects on the Thermodynamics of Electron Transfer. *J. Phys. Chem. B* **1999,** 103 (32), 6713-6722 DOI: 10.1021/jp991381+.

52.   Chattopadhyay, B.; Dannatt, J. E.; Andujar-De Sanctis, I. L.; Gore, K. A.; Maleczka, R. E.; Singleton, D. A.; Smith, M. R. Ir-Catalyzed ortho-Borylation of Phenols Directed by Substrate–Ligand Electrostatic Interactions: A Combined Experimental/in Silico Strategy for Optimizing Weak Interactions. *J. Am. Chem. Soc.* **2017,** 139 (23), 7864-7871 DOI: 10.1021/jacs.7b02232.

53.   Greenaway, K.; Dambruoso, P.; Ferrali, A.; Hazelwood, A. J.; Sladojevich, F.; Dixon, D. J. Enantioselective Organocatalytic Aryloxylation of β-Keto Esters. *Synthesis* **2011,** 2011 (12), 1880-1886.

TOC:

R = –OMe
TOF_{max} = 587 s^{-1}
FE_{HCOO^-} = 85%

R = –OH
TOF_{max} = 436 s^{-1}
FE_{HCOO^-} = 70%

CO_2

HCO_2^-

Relay effect enhances proton transfer

TOC Synopsis (71 words):

We report the synthesis, structural characterization, and reactivity of two iron(III) compounds with pendent –OMe and –OH groups for the electrocatalytic reduction of CO_2 to formate. Mechanistic studies suggest that the O atoms in the secondary coordination sphere are important for relaying exogeneous protons to the active site. These results indicate that using secondary sphere moieties to modulate metal-ligand interactions can be a powerful strategy for modulating electrocatalytic activity and selectivity.

26

Supporting Information for

Electrocatalytic CO$_2$ Reduction to Formate with Molecular Fe(III) Complexes Containing Pendent Proton Relays

Asa W. Nichols, Shelby L. Hooe, Joseph S. Kuehner,

Diane A. Dickie and Charles W. Machan*

Department of Chemistry, University of Virginia, PO Box 400319,

Charlottesville, VA 22904-4319.

* - machan@virginia.edu; ORCID 0000-0002-5182-1138

Determination of TOF_{max}

Calculation of TOF$_{max}$

$$TOF_{max} = 0.1992 \frac{n_p^3}{n_{cat}^2} \frac{Fv}{RT} \left(\frac{i_{cat}}{i_p}\right)^2$$

Where n_p is the number of electrons transferred under faradaic conditions, n_{cat} is the number of electrons transferred under catalytic conditions, R is the ideal gas constant, F is Faraday's constant, v is the scan rate, T is temperature, i_{cat} is the catalytic current, and i_p is the faradaic current. By plotting i_{cat}/i_p vs $v^{-1/2}$, the slope of the linear region can be used to determine TOF$_{max}$:

$$Slope = \frac{n_{cat}}{n_p^{3/2}} \frac{1}{0.4663} \sqrt{\frac{RT}{F}} TOF_{max}$$

$$TOF_{max} = 0.1992(slope)^2 \frac{n_p^3}{n_{cat}^2} \frac{F}{RT}$$

For the production of formate, $n_{cat} = 2$. We chose the first reduction feature i_p; $n_p = 1$.

Adapted from: F. Franco, M. F. Pinto, B. Royo, J. Lloret-Fillol, *Angew. Chem. Int. Ed.* **2018**, *57*, 4603.
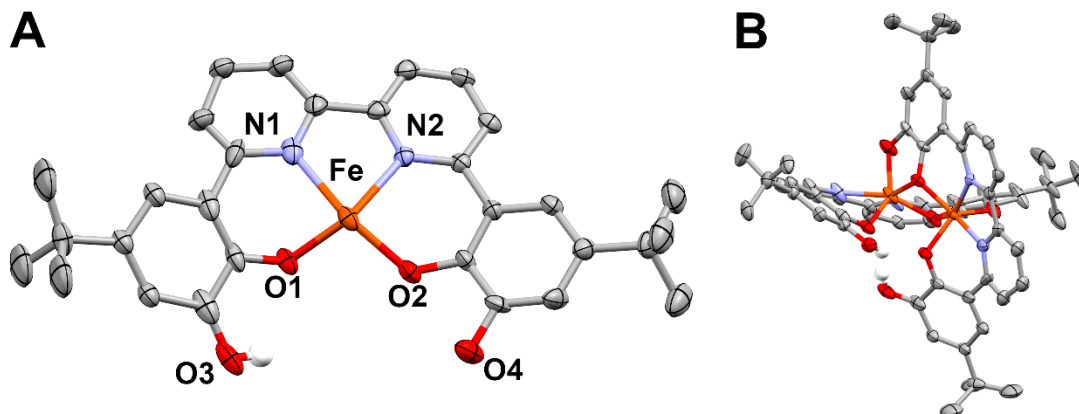
Figure S1. (**A**) Representative monomer structure (one of two structurally inequivalent units crystallographically) from (**B**) overall dimer structure of **3**. C = grey, O = red, N= blue, Fe = orange. Thermal ellipsoids set to 30%. Non-catecholate H-atoms, occluded MeCN and second set of coordinates for disordered *tert*-butyl groups and bpy ring omitted for clarity.
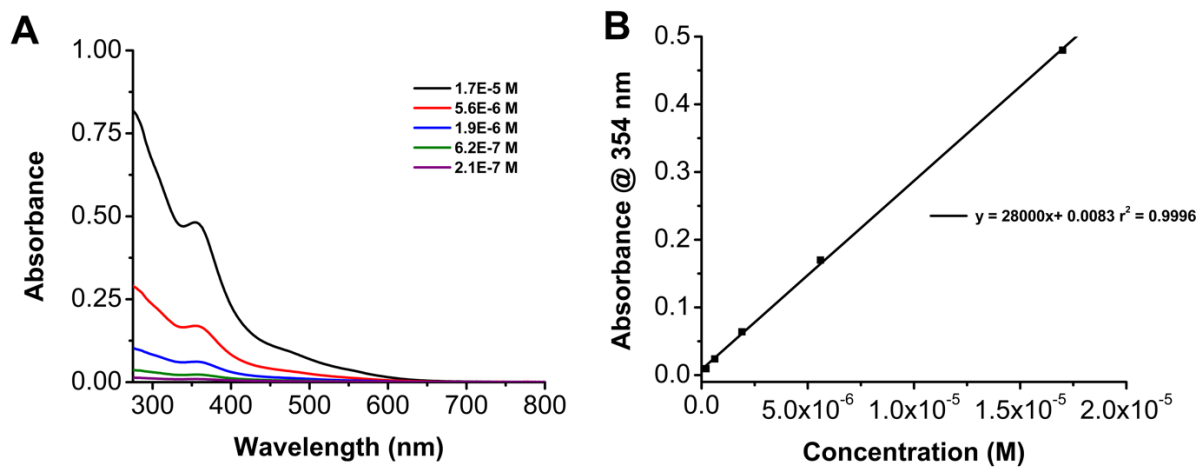
Figure S2. UV-Vis absorbance spectra of serial dilutions of **2** in *N,N*-DMF showing absence of equillibrium processes. Pathlength 1 cm.
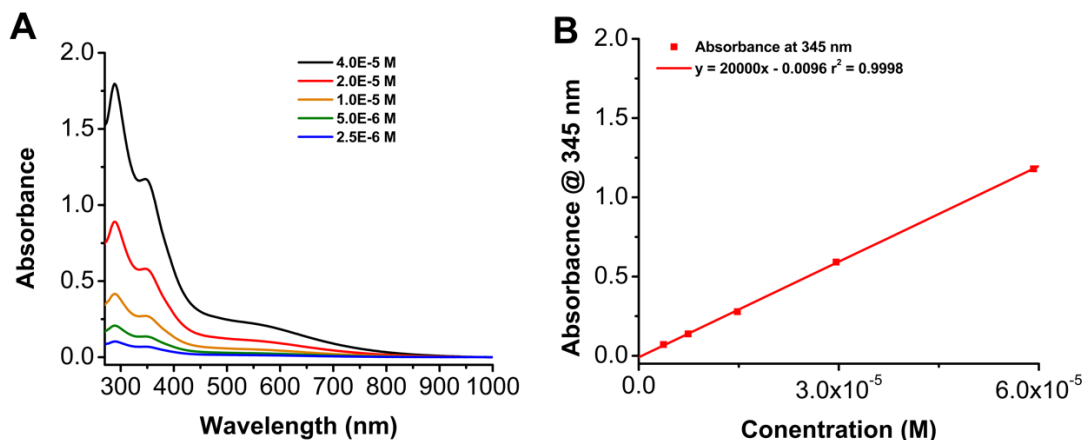
Figure S3. UV-Vis absorbance spectra of serial dilutions of **3** in *N,N*-DMF showing absence of equillibrium processes. Pathlength 1 cm.
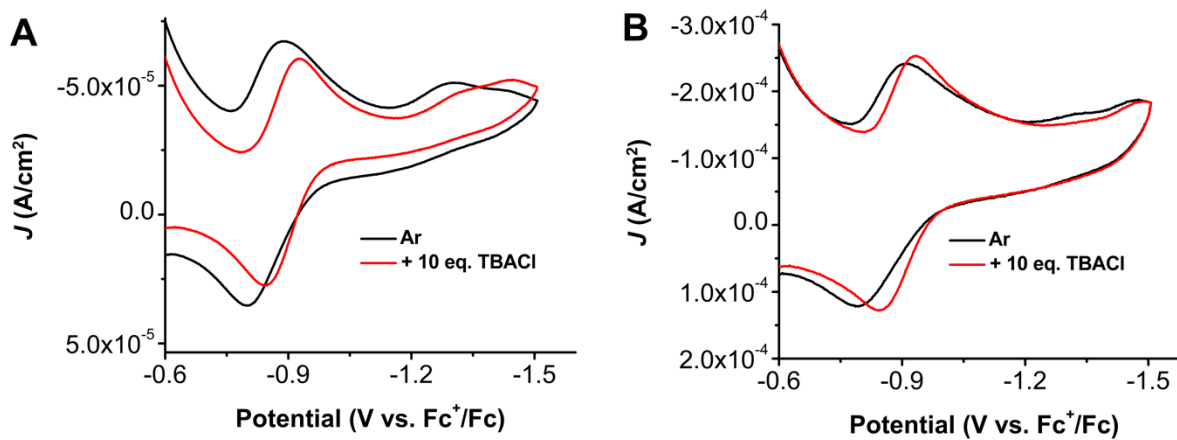
Figure S4. CVs of Fe(^{me}crebpy)Cl **2** upon addition of TBACl. At fast scan rates, reduction at – 1.45 V vs Fc$^+$/Fc dissapears. (**A**) 100 mV/s. (**B**) 1000 mV/s. Glassy carbon working and counter electrodes, Ag/AgCl pseudoreference electrode, referenced to internal decamethylferrocene Cp$_2$*Fe standard.
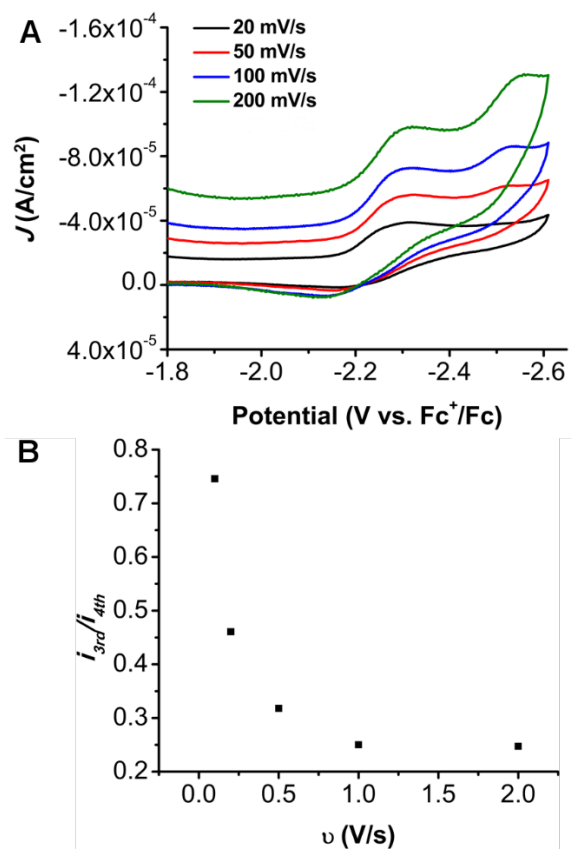
Figure S5. (**A**) Plots of 3rd and 4th reduction potentials of **3** showing scan rate dependence of the relative current response of these two features. (**B**) Plot of the ratio of the peak current of the 3rd and 4th reductions of **3** vs. scan rate. Glassy carbon working and counter electrodes, Ag/AgCl pseudoreference electrode, referenced to internal $Cp_2{}^*Fe$ standard.
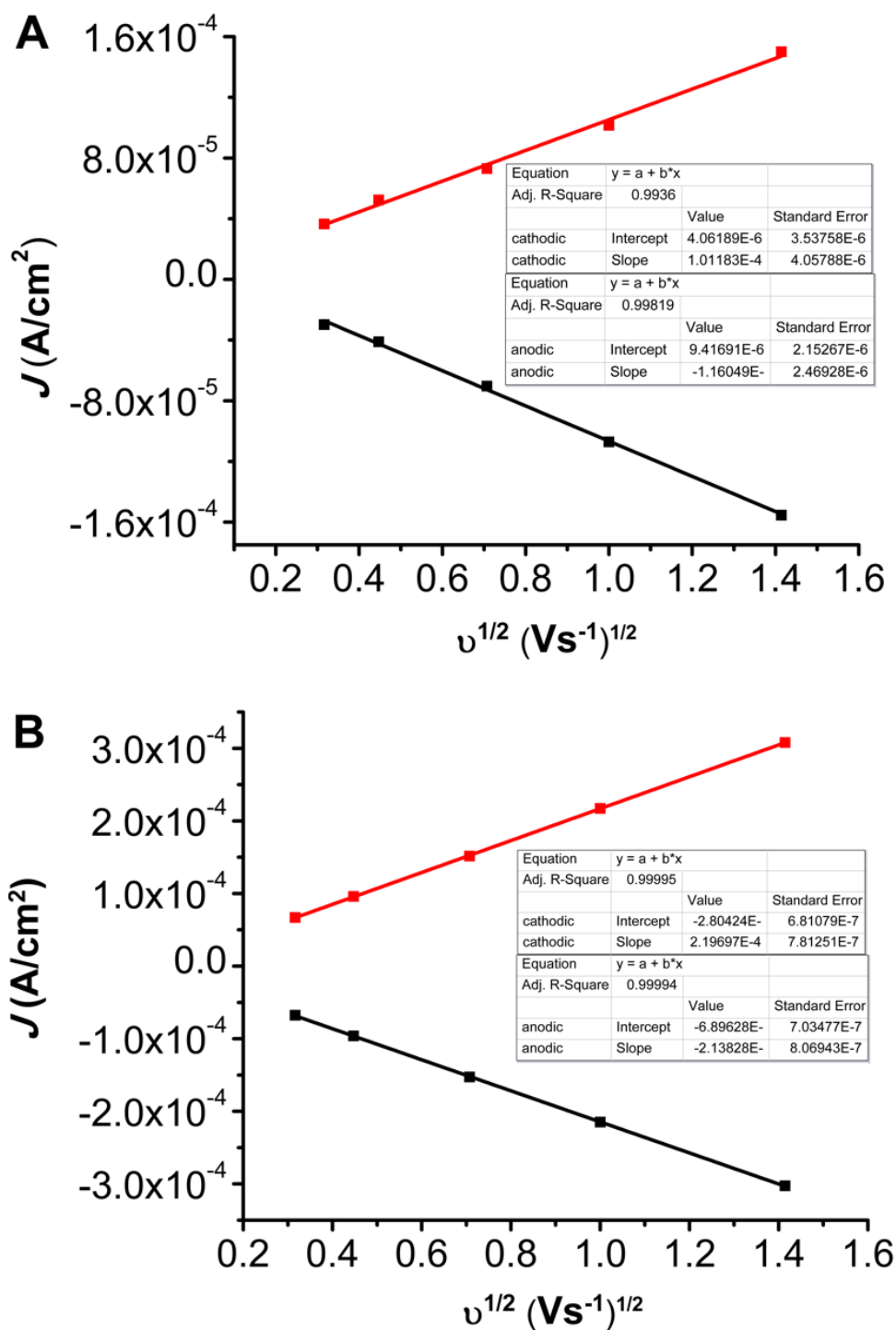
Figure S6. Plots of current density vs $\upsilon^{1/2}$ for the reductions with $E_{1/2}$ = -0.84 V (**A**) and -1.93 V (**B**) vs Fc+/Fc for **2**. Linearity indicates **2** is operating in a diffusion limited regime. Glassy carbon working and counter electrodes, Ag/AgCl pseudoreference electrode, referenced to internal Cp_2*Fe standard.

A

Equation	y = a + b*x	
Adj. R-Square	0.99716	0.9845
		Value	Standard Error
cathodic	Intercept	4.81046E-6	2.66555E-6
cathodic	Slope	-1.14682E-4	3.05759E-6
anodic	Intercept	-6.86478E-6	6.32666E-6
anodic	Slope	1.15921E-4	7.25718E-6

B

Equation	y = a + b*x	
Adj. R-Square	0.99716	0.9845
		Value	Standard Error
cathodic	Intercept	4.81046E-6	2.66555E-6
cathodic	Slope	-1.14682E-4	3.05759E-6
anodic	Intercept	-6.86478E-6	6.32666E-6
anodic	Slope	1.15921E-4	7.25718E-6
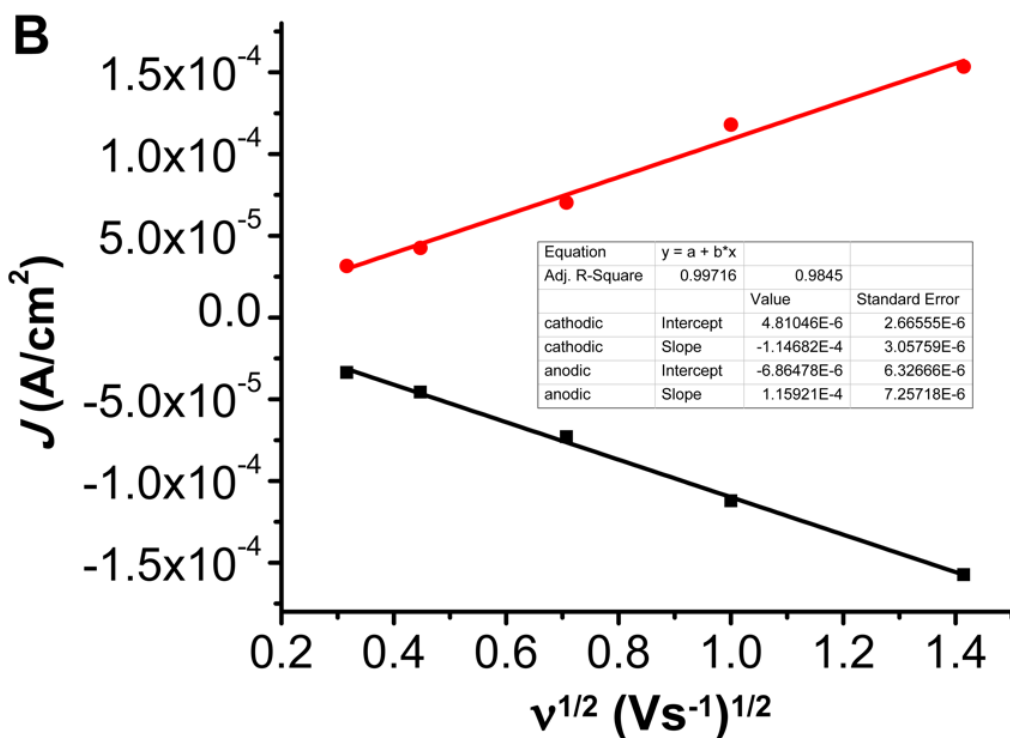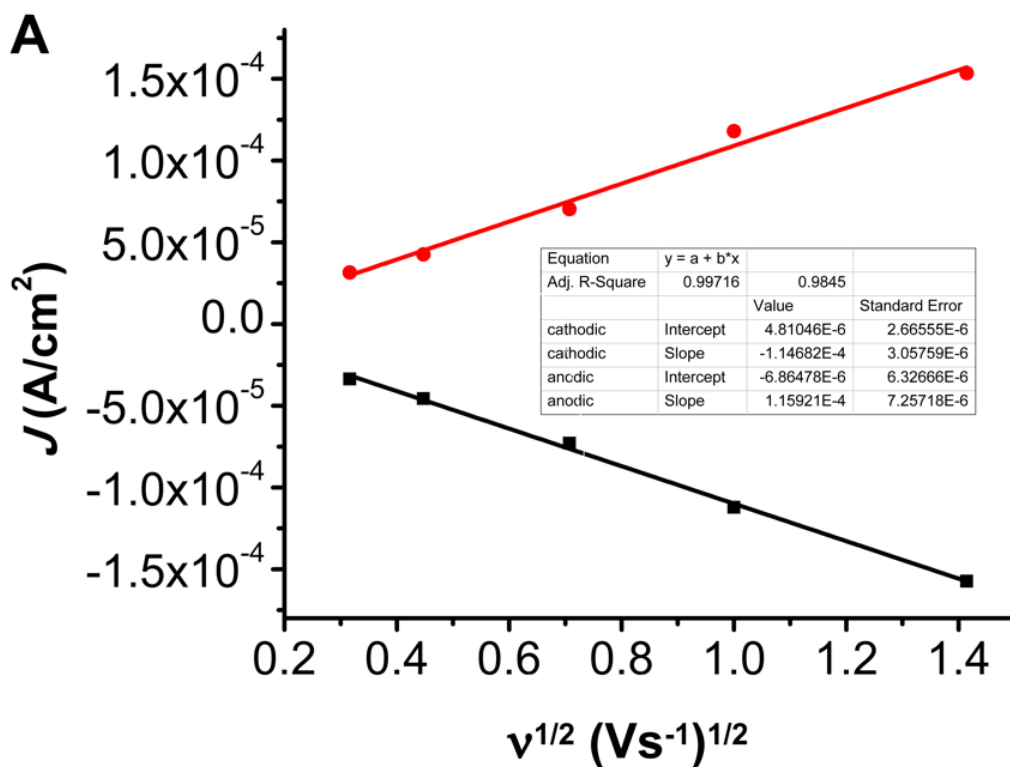
Figure S7. Plots of current density vs $\upsilon^{1/2}$ for the reductions with $E_{1/2}$ = -1.01 V (**A**) and -1.65 V (**B**) vs Fc^+/Fc for **3**. Linearity indicates **3** is operating in a diffusion limited regime. Glassy carbon working and counter electrodes, Ag/AgCl pseudoreference electrode, referenced to internal Cp_2*Fe standard.
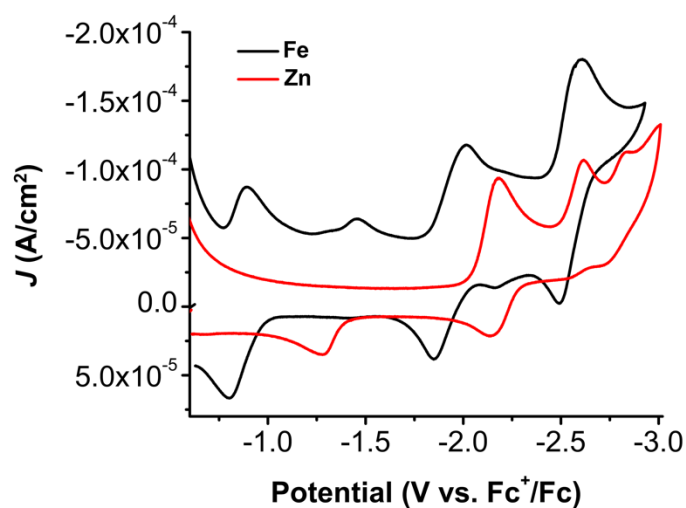
Figure S8. Cyclic voltammogram of 0.5 mM **2** or Zn(^{me}crebpy) in 0.1 M TBAPF$_6$/*N,N*-DMF supporting electrolyte under Ar saturation conditions. Glassy carbon working and counter electrodes, Ag/AgCl pseudoreference electrode, referenced to internal Cp$_2$*Fe standard, 100 mV/s scan rate.
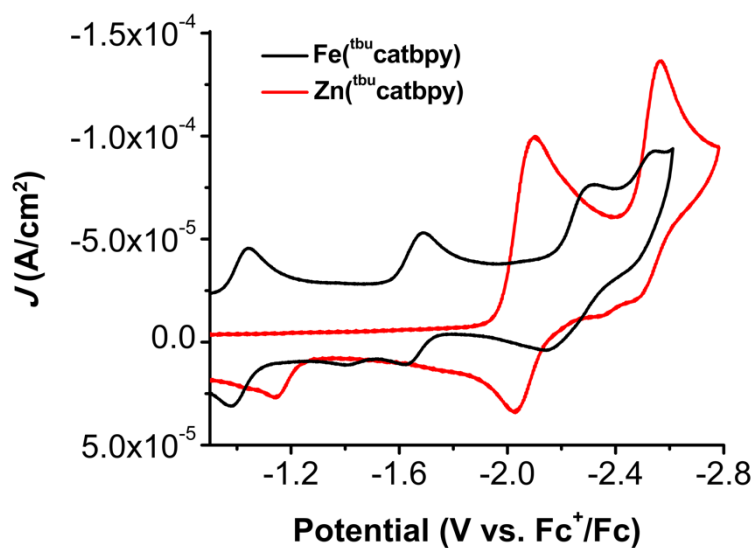

Figure S9. Cyclic voltammogram of 0.5 mM **3** or Zn(^{tbu}catbpy) in 0.1 M TBAPF$_6$/*N,N*-DMF supporting electrolyte under Ar saturation conditions. Glassy carbon working and counter electrodes, Ag/AgCl pseudoreference electrode, referenced to internal Cp$_2$*Fe or Cp$_2$Co standard, 100 mV/s scan rate.
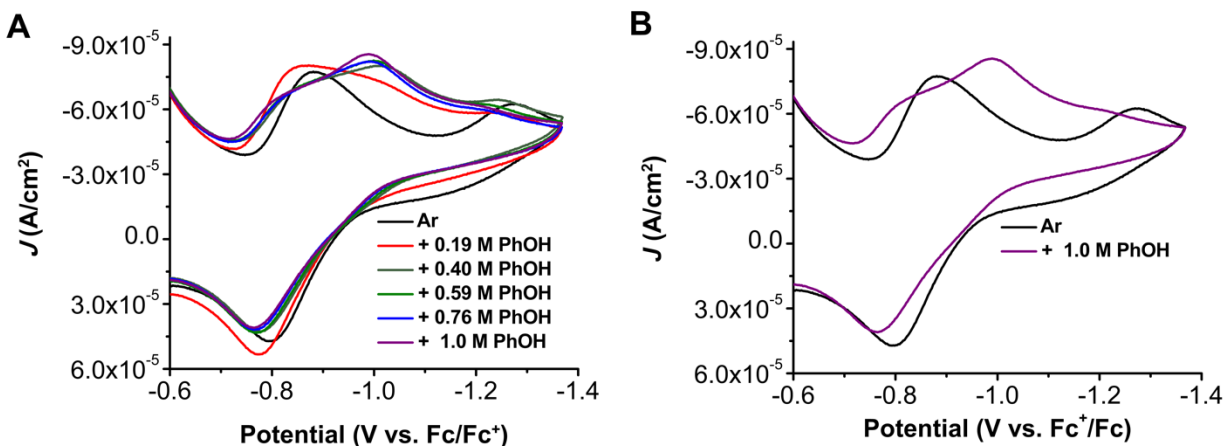
Figure S10. Cyclic voltammograms of 0.5 mM **2** in 0.1 M TBAPF$_6$/*N,N*-DMF supporting electrolyte under Ar saturation conditions with varied amounts of PhOH showing a shift in the first two reduction features. Glassy carbon working and counter electrodes, Ag/AgCl pseudoreference electrode, referenced to internal Cp$_2$*Fe standard, 100 mV/s scan rate.
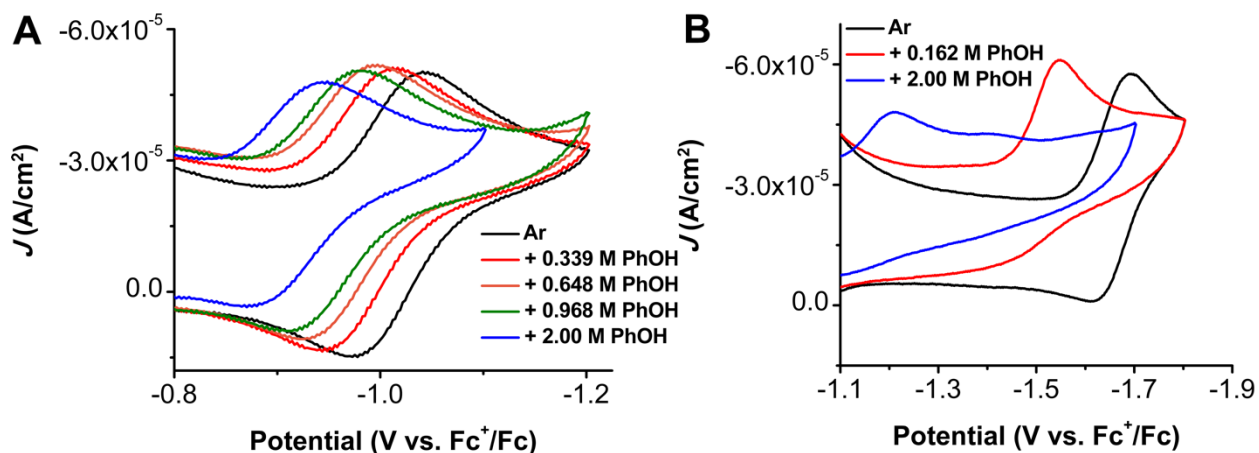
**Figure S11.** Cyclic voltammograms of 0.5 mM **3** in 0.1 M TBAPF$_6$/*N,N*-DMF supporting electrolyte under Ar saturation conditions with varied amounts of PhOH showing a shift in the first two reduction features. Glassy carbon working and counter electrodes, Ag/AgCl pseudoreference electrode, referenced to internal Cp$_2$*Fe standard, 100 mV/s scan rate.
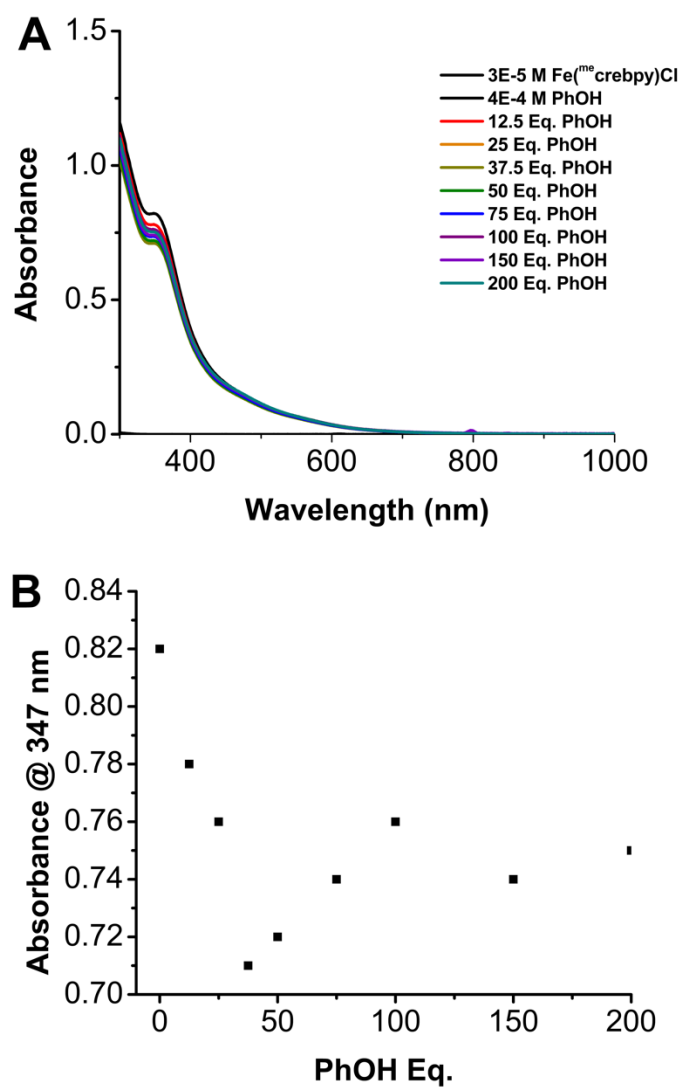
Figure S12. UV-Vis titration of PhOH into a solution of Fe(^{me}crebpy)Cl **2**. Pathlength = 1 cm.
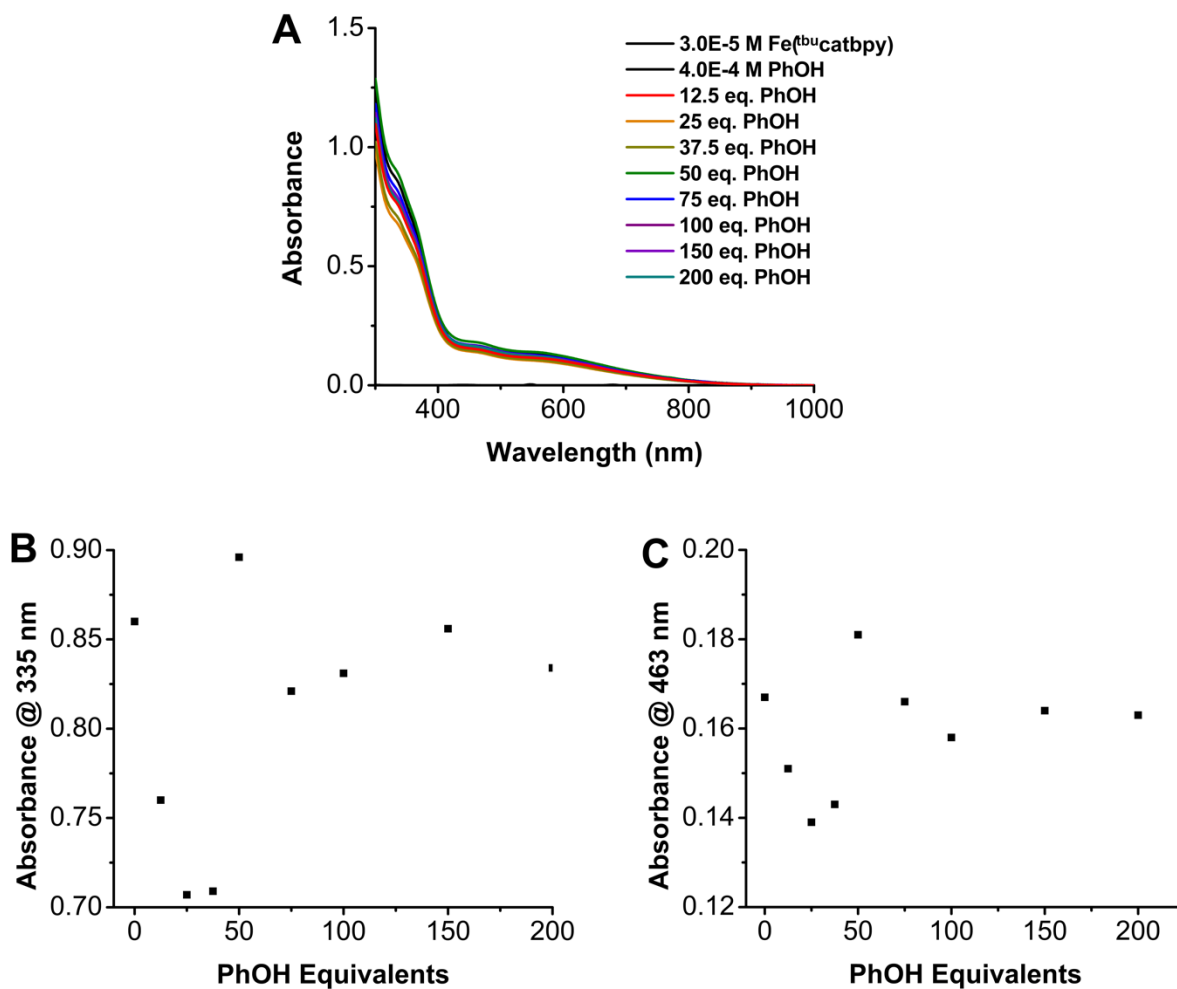
Figure S13. UV-Vis titration of PhOH into a solution of Fe(^{tbu}catbpy). Pathlength = 1 cm.
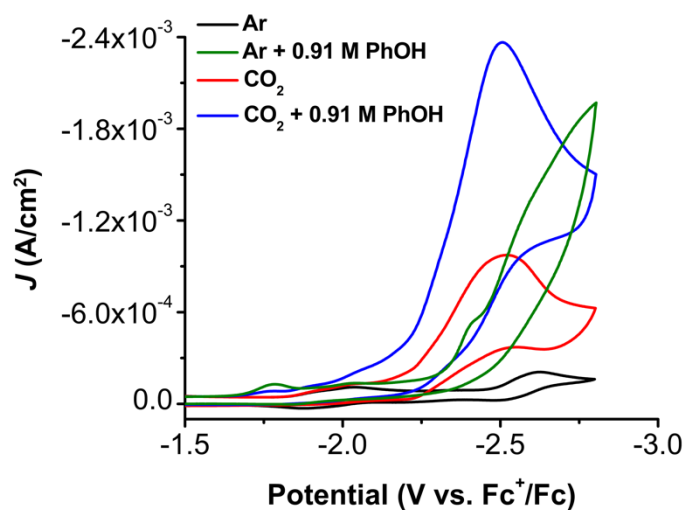
Figure S14. Cyclic voltammograms of 0.5 mM **2** in 0.1 M TBAPF$_6$/*N,N*-DMF supporting electrolyte under labeled conditions. Glassy carbon working and counter electrodes, Ag/AgCl pseudoreference electrode, referenced to internal Cp$_2$*Fe standard, 100 mV/s scan rate.
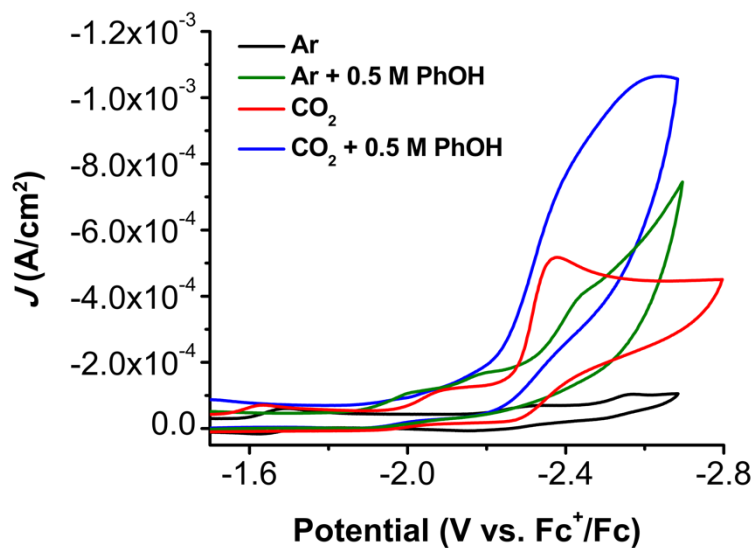

Figure S15. Cyclic voltammograms of 0.5 mM **3** in 0.1 M TBAPF$_6$/*N,N*-DMF supporting electrolyte under labeled conditions. Glassy carbon working and counter electrodes, Ag/AgCl pseudoreference electrode, referenced to internal Cp$_2$*Fe standard, 100 mV/s scan rate.
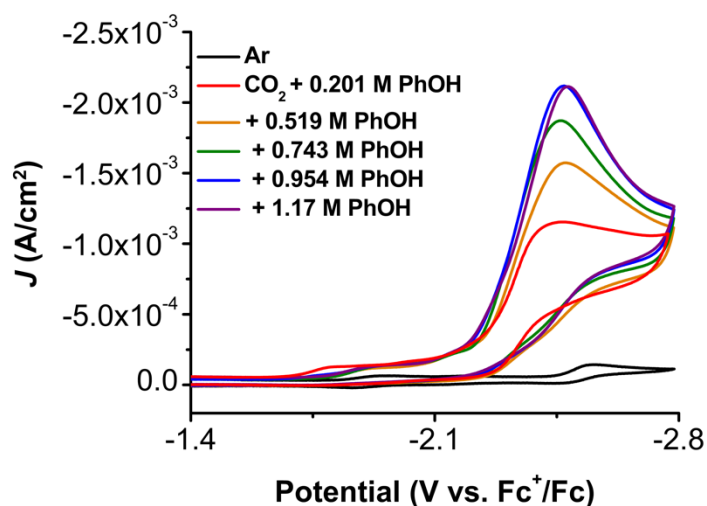
Figure S16. Cyclic Voltammograms of 0.5 mM Fe(^{me}crebpy)Cl **2** in 0.1 M TBAPF$_6$/N,N-DMF supporting electrolyte with scans to the catalytic wave showing current saturation occurs at ~0.9 M PhOH. Glassy carbon working and counter electrodes, Ag/AgCl pseudoreference electrode, referenced to internal Cp$_2$*Fe standard, 100 mV/s scan rate.
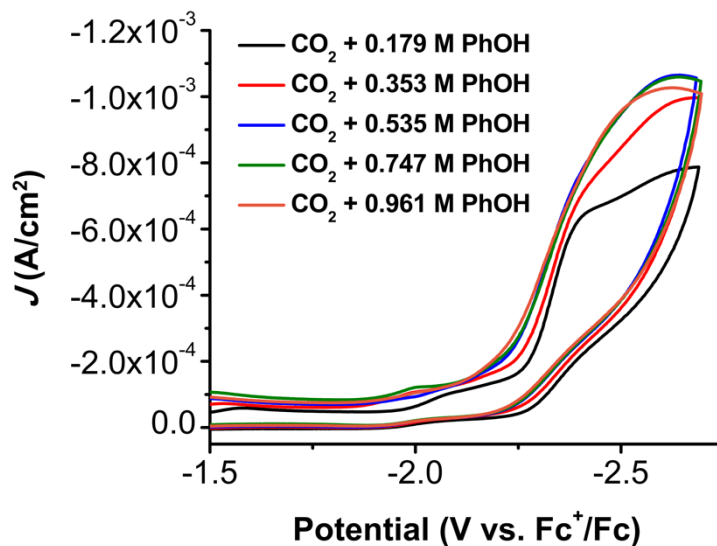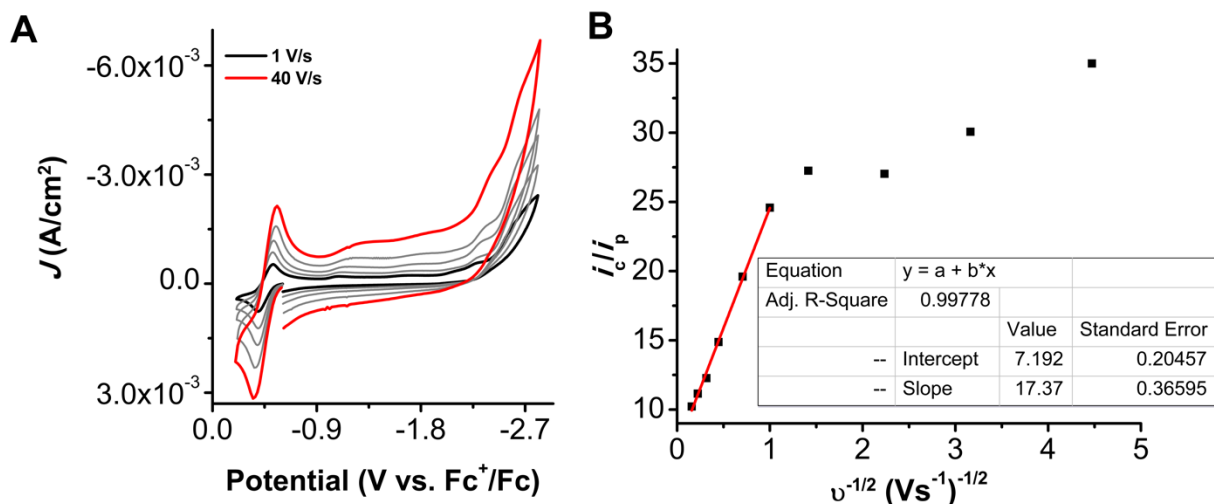

Figure S17. Cyclic Voltammograms of 0.5 mM Fe(^{tbu}catbpy) **3** in 0.1 M TBAPF$_6$/N,N-DMF supporting electrolyte with scans to the catalytic wave showing current saturation occurs at 0.5 M PhOH. Glassy carbon working and counter electrodes, Ag/AgCl pseudoreference electrode, referenced to internal Cp$_2$*Fe standard, 100 mV/s scan rate.
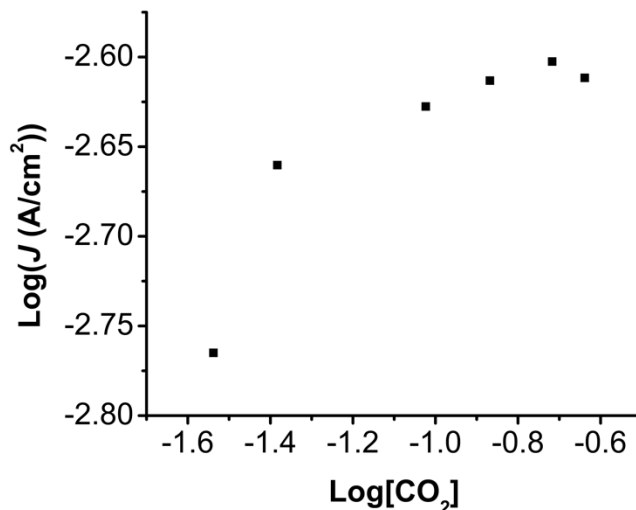
Figure S18. Log-log plot of current density and $[CO_2]$ for 0.5 mM **2**, Fe(^{me}crebpy)Cl with 1.0 M PhOH. Kinetic current saturation is observed above 0.04 M CO_2. Glassy carbon working and counter electrodes, Ag/AgCl pseudoreference electrode, referenced to internal Cp_2*Fe standard, 100 mV/s scan rate.
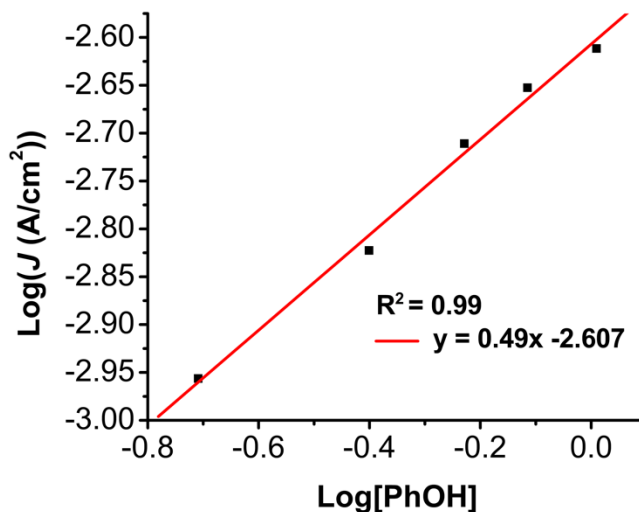
Figure S19. Log-log plot of current density and [PhOH] for 0.5 mM **2**, Fe(^{tbu}catbpy) under CO_2 saturation conditions. Slope of 0.5 is indicative of 1st order kinetics with respect to [PhOH]. Glassy carbon working and counter electrodes, Ag/AgCl pseudoreference electrode, referenced to internal Cp_2*Fe standard, 100 mV/s scan rate.
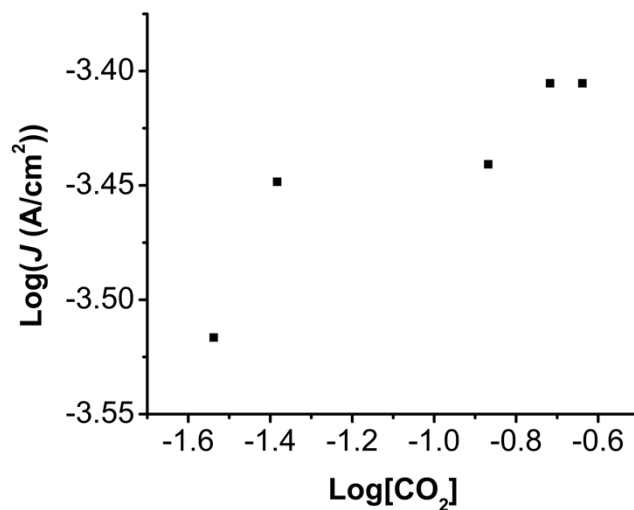
**Figure S20**. Log-log plot of current density and [CO_2] for 0.5 mM **3**, Fe(^{tbu}catbpy) with 0.5 M PhOH. Kinetic current saturation is observed above 0.04 M CO_2. Glassy carbon working and counter electrodes, Ag/AgCl pseudoreference electrode, referenced to internal Cp$_2$*Fe standard, 100 mV/s scan rate.
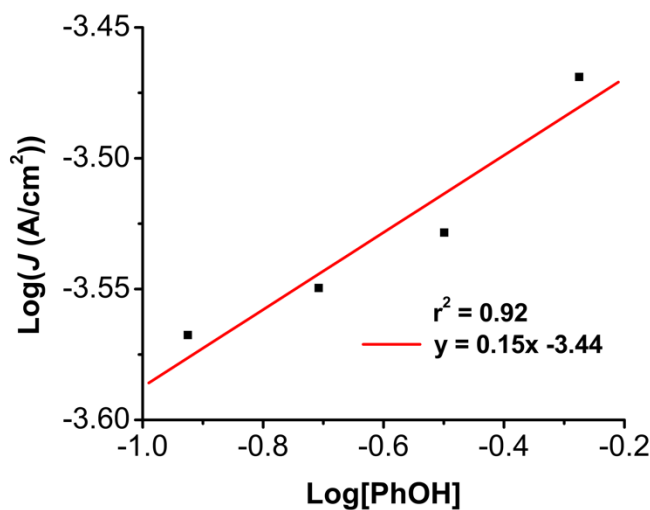

Figure S21. Log-log plot of current density and [PhOH] for 0.5 mM **3**, Fe(^{me}crebpy)Cl under CO_2 saturation conditions. Slope of 0.5 is indicative of 1st order kinetics with respect to [PhOH]. Glassy carbon working and counter electrodes, Ag/AgCl pseudoreference electrode, referenced to internal Cp$_2$*Fe standard, 100 mV/s scan rate.
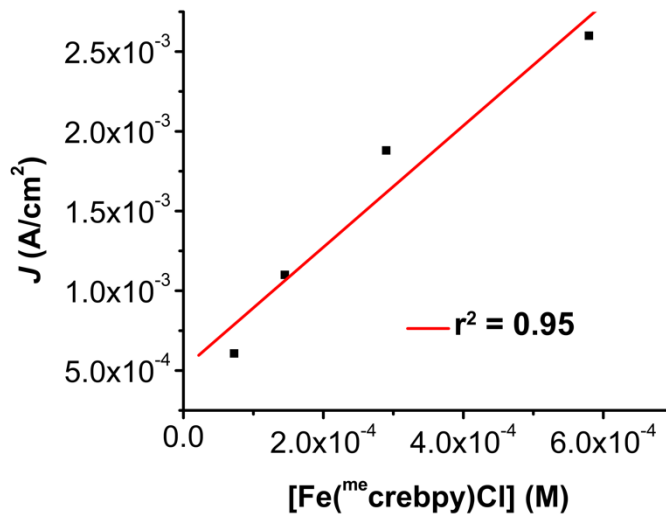
Figure S22. Plot of current density and [**2**], Fe(^{me}crebpy)Cl under CO_2 saturation conditions with 1.0 M PhOH. Linearity is consistent with 1st order kinetics with respect to [**2**]. Glassy carbon working and counter electrodes, Ag/AgCl pseudoreference electrode, referenced to internal Cp$_2$*Fe standard, 100 mV/s scan rate.
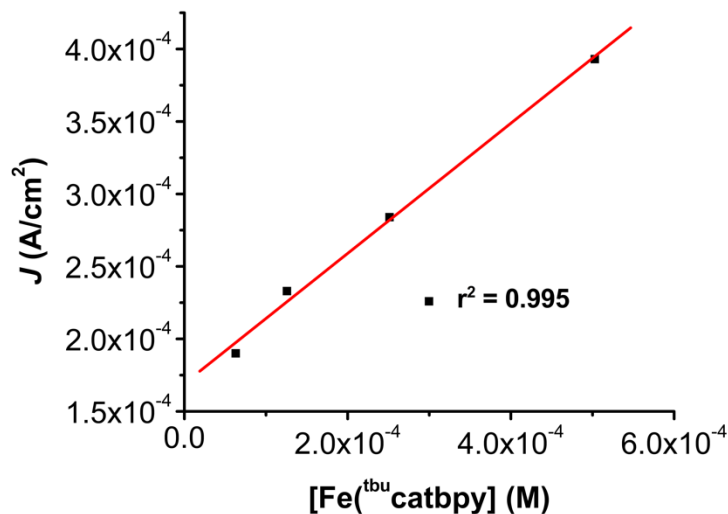
Figure S23. Plot of current density and [**3**], Fe(^{tbu}catbpy) under CO_2 saturation conditions with 0.5 M PhOH. Linearity is consistent with 1st order kinetics with respect to [**3**]. Glassy carbon working and counter electrodes, Ag/AgCl pseudoreference electrode, referenced to internal Cp$_2$*Fe standard, 100 mV/s scan rate.

Figure S24. (**A**) Cyclic voltammograms and (**B**) plot of i_c/i_p vs $\upsilon^{-1/2}$ for 0.5 mM Fe(^{me}crebpy)Cl **2** under saturated CO_2 conditions with 0.54 M PhOH in 0.1 M TBAPF$_6$/*N,N*-DMF supporting electrolyte. Glassy carbon working and counter electrodes, Ag/AgCl pseudoreference electrode, referenced to internal Cp$_2$*Fe standard. Linear region of plot used to determine TOF$_{max}$ by a previously reported procedure.[5]
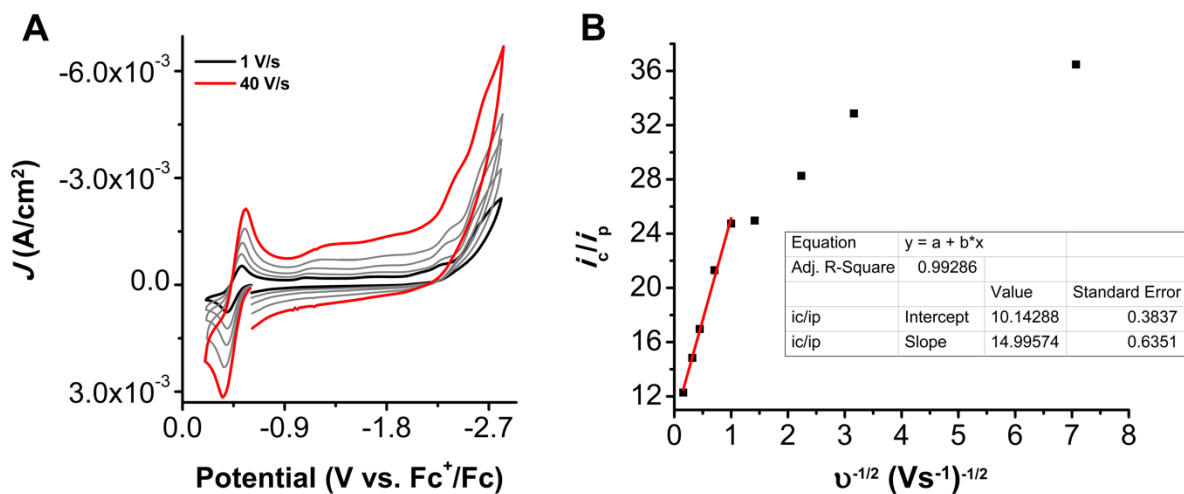

Figure S25. (**A**) Cyclic voltammograms and (**B**) plot of i_c/i_p vs $\upsilon^{-1/2}$ for 0.5 mM Fe(^{tbu}catbpy) **3** under saturated CO_2 conditions with 0.51 M PhOH in 0.1 M TBAPF$_6$/*N,N*-DMF supporting electrolyte. Glassy carbon working and counter electrodes, Ag/AgCl pseudoreference electrode, referenced to internal Cp$_2$*Fe standard, 100 mV/s scan rate. Linear region of plot used to determine TOF$_{max}$ by a previously reported procedure.[5]
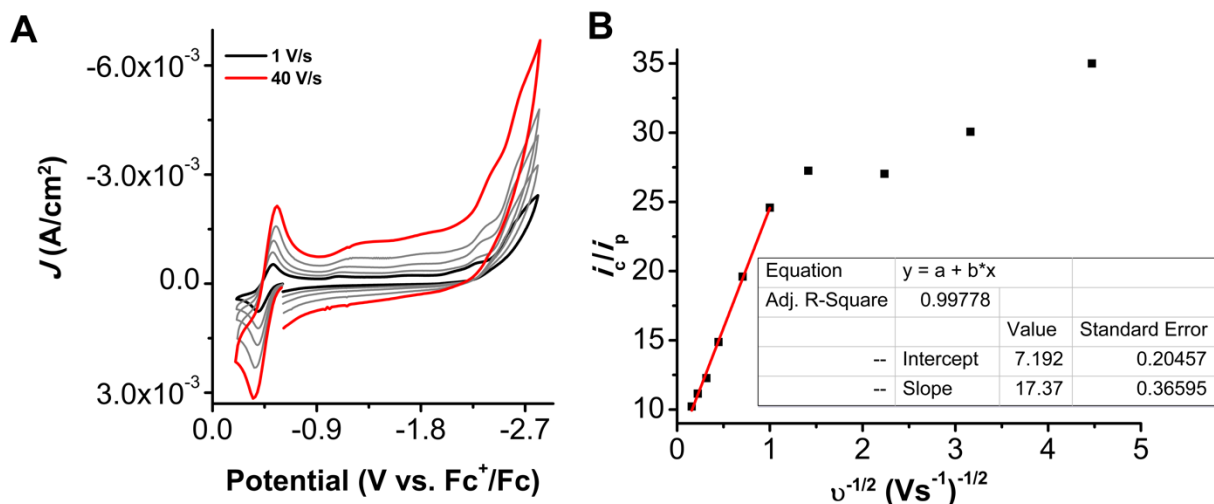
Figure S26. (**A**) Cyclic voltammograms and (**B**) plot of i_c/i_p vs $\upsilon^{-1/2}$ for 0.5 mM Fe(^{me}crebpy)Cl **2** under saturated CO_2 conditions with 1.0 M PhOH in 0.1 M TBAPF$_6$/N,N-DMF supporting electrolyte Glassy carbon working and counter electrodes, Ag/AgCl pseudoreference electrode, referenced to internal Cp$_2$*Fe standard. Linear region of plot used to determine TOF$_{max}$ by a previously reported procedure.[5]
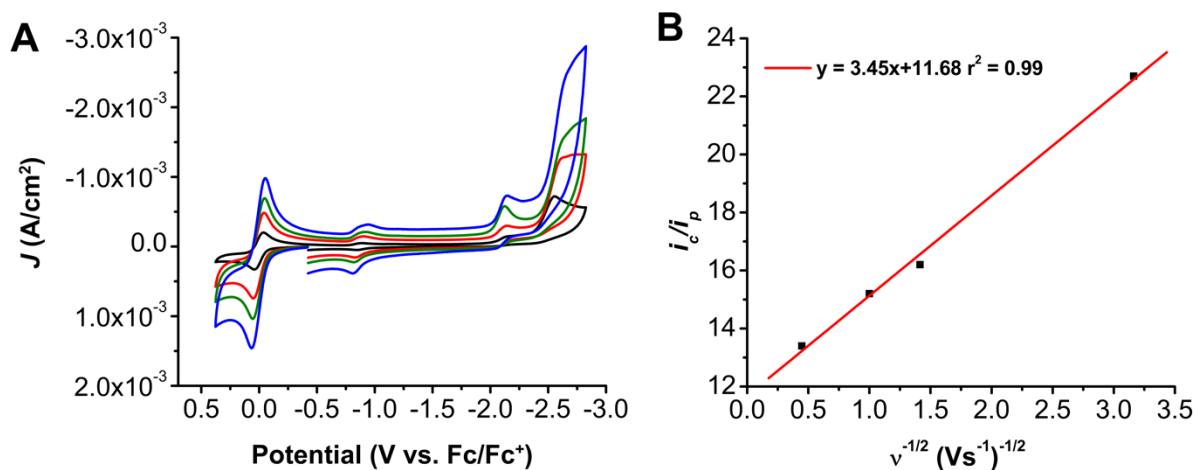
Figure S27. (**A**) Cyclic voltammograms and (**B**) plot of i_c/i_p vs $\upsilon^{-1/2}$ for 0.5 mM Fe(^{tbu}dhbpy)Cl **1** under saturated CO_2 conditions with 0.5 M PhOH in 0.1 M TBAPF$_6$/N,N-DMF supporting electrolyte Glassy carbon working and counter electrodes, Ag/AgCl pseudoreference electrode, referenced to internal Cp$_2$Fe standard. Linear region of plot used to determine TOF$_{max}$ by a previously reported procedure.[5] Scan rates are 0.1 (black), 0.5 (red), 1.0 (green), and 5.0 (blue) V/s.
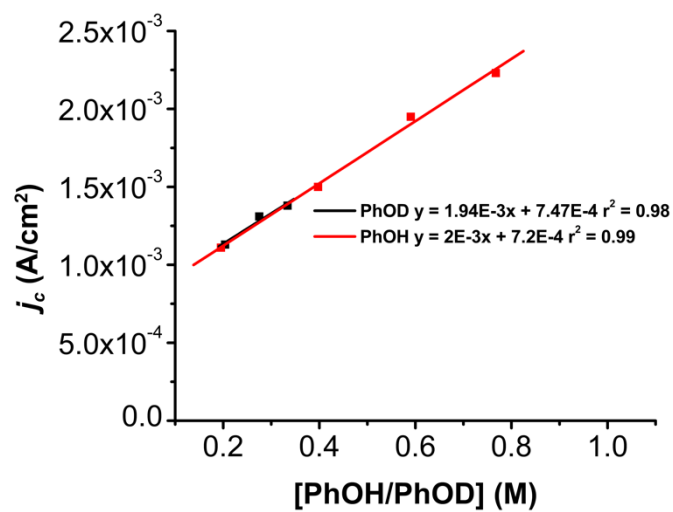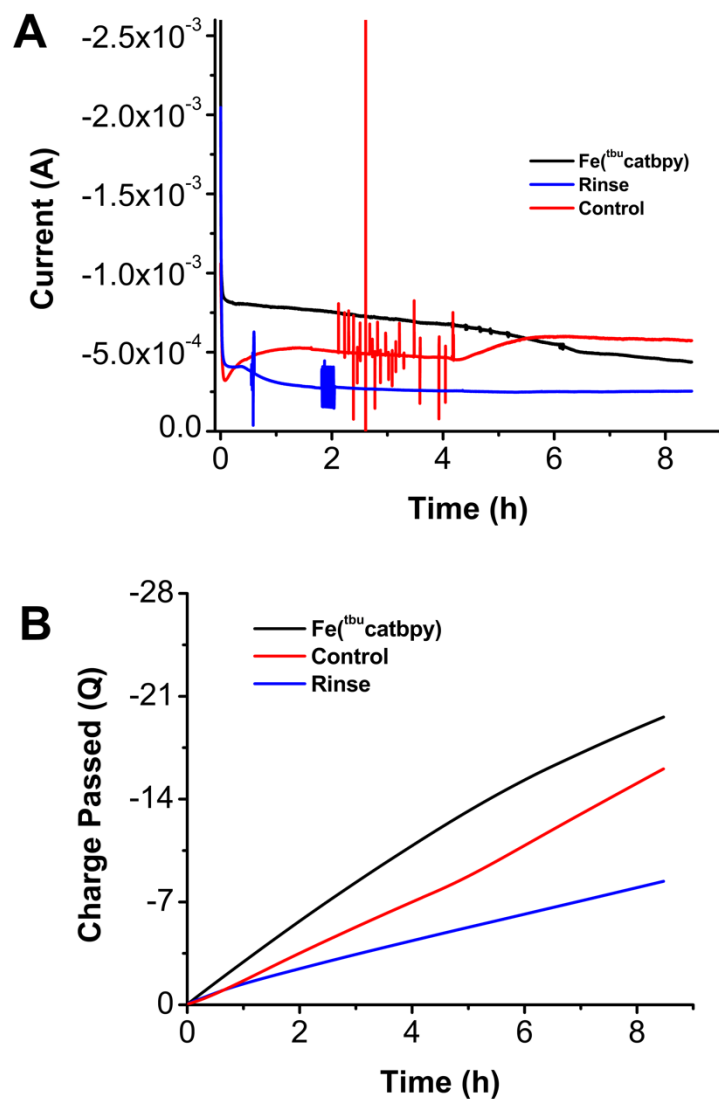
**Figure S28.** Plot used to determine KIE for **Fe(^{me}crebpy)Cl 2.**
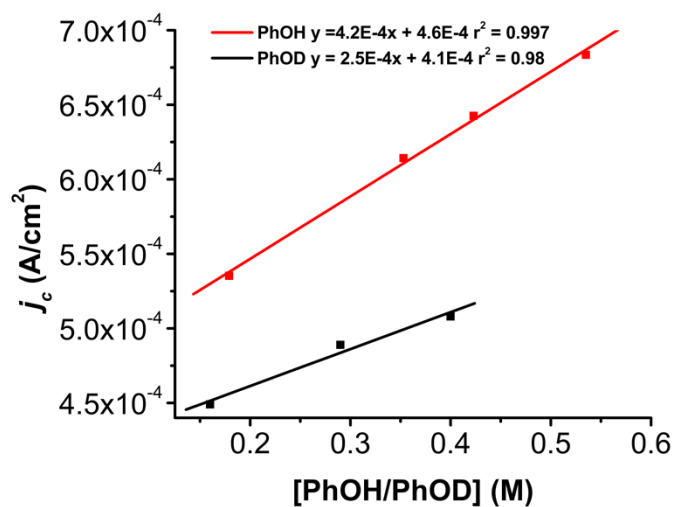
Figure S29. Plot used to determine KIE for **Fe(^{tbu}catbpy) 3**.
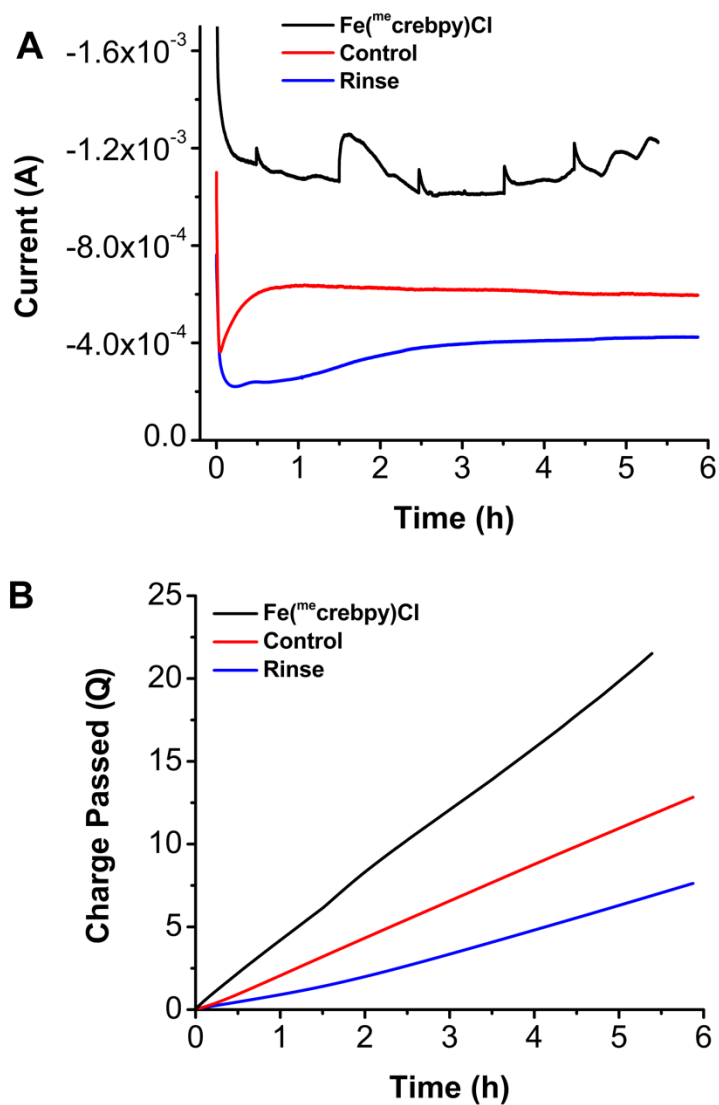
Figure S30. Current vs. Time and Charge Passed vs. Time Plots for CPE experiments at –2.50 V vs Fc^+/Fc with 0.5 mM $Fe(^{me}crebpy)Cl$ **2**, 0.9 M PhOH, and CO_2 atmosphere. Graphite working and counter electrodes were used.

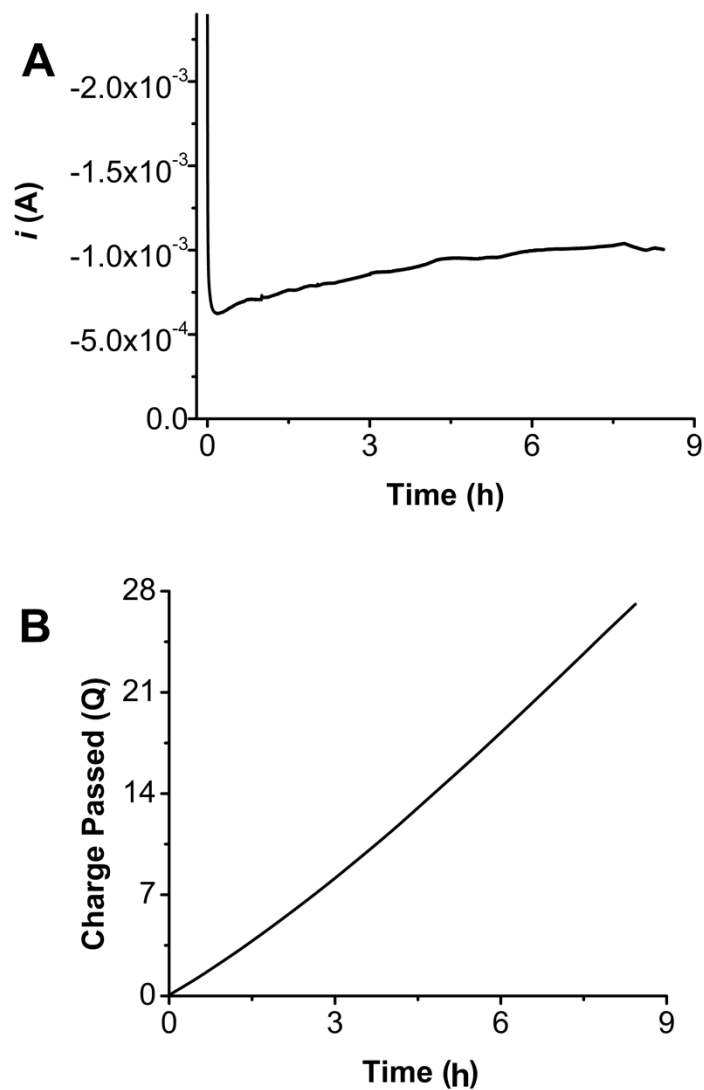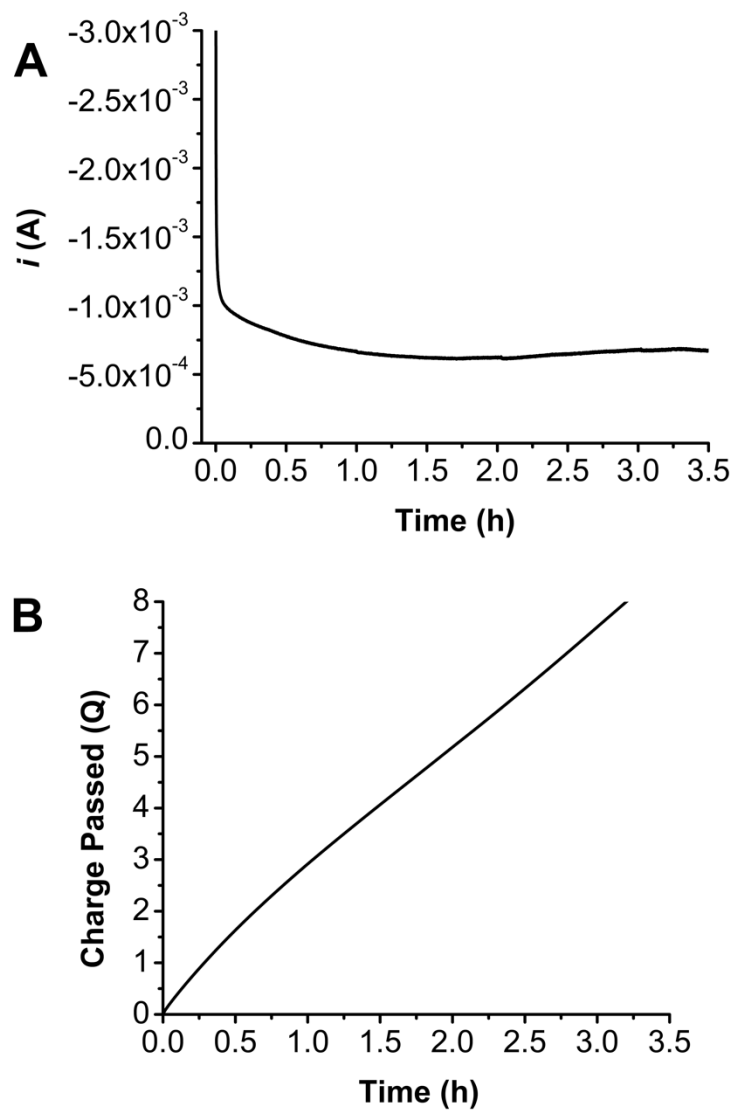**Figure S31.** Current vs. Time (**A**) and Charge Passed vs. Time plots (**B**) for CPE experiments at –2.60 V vs Fc$^+$/Fc with 0.5 mM Fe(^{tbu}catbpy) **3**, 0.5 M PhOH, and CO$_2$ atmosphere. Graphite working and counter electrodes were used.
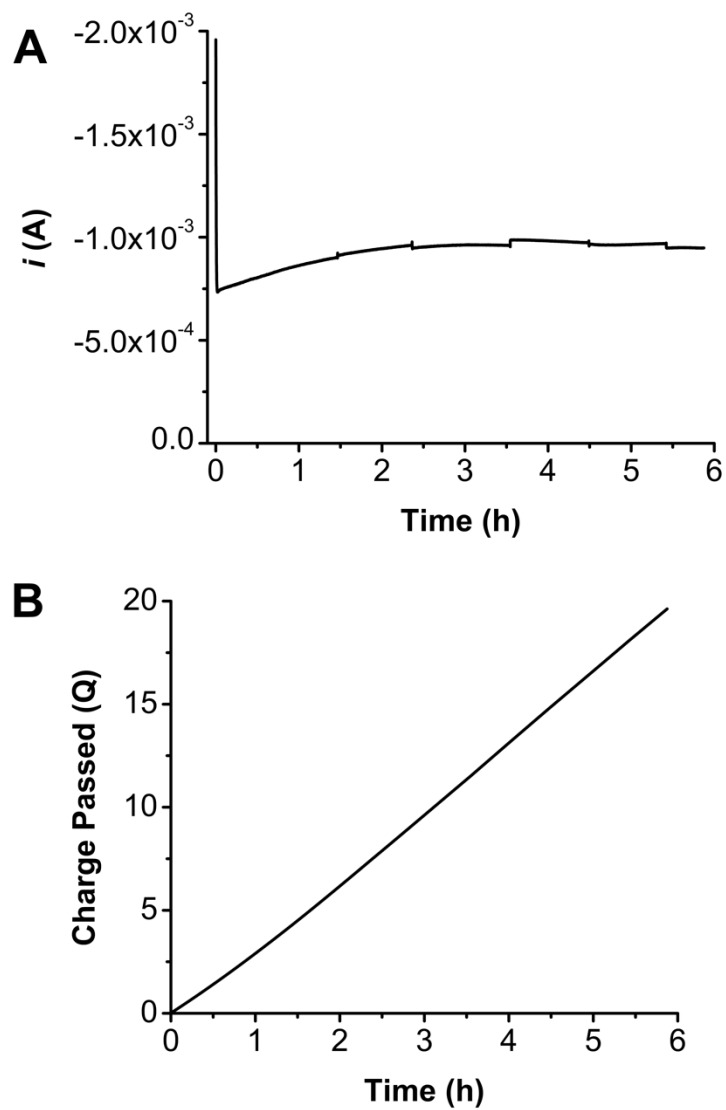
Figure S32. Current vs. Time (**A**) and Charge Passed vs. Time plots (**B**) for CPE experiments at –2.60 V vs Fc$^+$/Fc with 0.5 mM Fe(^{me}crebpy)Cl **3**, 0.9 M PhOH, and Ar atmosphere. Graphite working and counter electrodes were used.

Figure S33. Current vs. Time (**A**) and Charge Passed vs. Time plots (**B**) for CPE experiments at –2.60 V vs Fc$^+$/Fc with 0.5 mM Fe(^{tbu}catbpy) **3**, 0.5 M PhOH, and Ar atmosphere. Graphite working and counter electrodes were used.

Figure S34. Current vs. Time (**A**) and Charge Passed vs. Time plots (**B**) for CPE experiments at –2.60 V vs Fc$^+$/Fc with 0.5 mM Fe(^{tbu}catbpy) **3** and Ar atmosphere. Graphite working and counter electrodes were used.
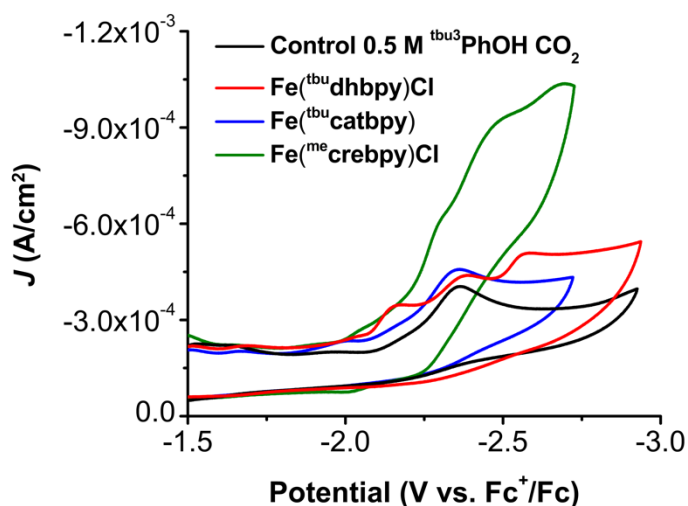
Figure S35. Cyclic Voltammograms of 0.5 mM Fe(^{tbu}dhbpy)Cl **1** (red), Fe(^{me}crebpy)Cl **2** (green)**,** and Fe(^{tbu}catbpy)Cl **3** (blue) in 0.1 M TBAPF$_6$/*N,N*-DMF supporting electrolyte with 0.5 M 2,4,6-tri-*tert*-butyl-phenol (^{tbu3}**PhOH**) under CO_2 saturation conditions. Control experiment is under identical conditions with no catalyst material added. Glassy carbon working and counter electrodes, Ag/AgCl pseudoreference electrode, referenced to internal Cp$_2$*Fe standard, 100 mV/s scan rate.
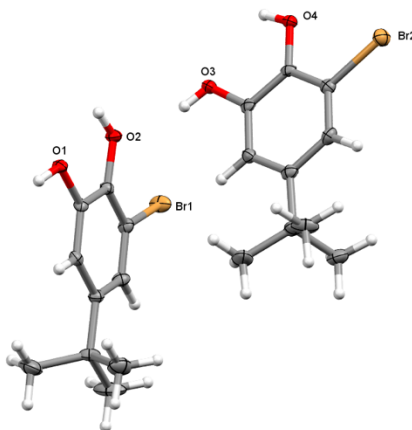
Figure S36. Crystal structure of 3-bromo-5-*tert*-butyl-benzene-diol. Grown by sublimation. Thermal ellipsoids set to 50%.

Table S1. Diffusion coefficients determined using the Randles-Sevcik equation and variable scan rate studies.[6] [a] - as determined at first reduction potential. [b] - as determined at second reduction potential.

Complex	Diffusion Coefficient[a] ($cm^2 s^{-1}$)	Diffusion Coefficient[b] ($cm^2 s^{-1}$)
1	4.88E-09	3.34E-09
2	7.47E-07	2.54E-06
3	5.37E-07	1.11E-09

References

1. A. W. Nichols, S. Chatterjee, M. Sabat and C. W. Machan, *Inorganic Chemistry*, 2018, **57**, 2111-2121.
2. I. Noviandri, K. N. Brown, D. S. Fleming, P. T. Gulyas, P. A. Lay, A. F. Masters and L. Phillips, *J. Phys. Chem. B*, 1999, **103**, 6713-6722.
3. B. Chattopadhyay, J. E. Dannatt, I. L. Andujar-De Sanctis, K. A. Gore, R. E. Maleczka, D. A. Singleton and M. R. Smith, *J. Am. Chem. Soc.*, 2017, **139**, 7864-7871.
4. K. Greenaway, P. Dambruoso, A. Ferrali, A. J. Hazelwood, F. Sladojevich and D. J. Dixon, *Synthesis*, 2011, **2011**, 1880-1886.
5. F. Franco, F. Pinto Mara, B. Royo and J. Lloret-Fillol, *Angew. Chem., Int. Ed.*, 2018, **57**, 4603-4606.
6. A. J. Bard and L. R. Faulkner, *Electrochemical Methods: Fundamentals and Applications*, John Wiley & Sons, Inc., Hoboken, NJ, 2nd edn., 2001.